

## RESEARCH ARTICLE

# Glioblastoma-derived extracellular vesicle subpopulations following 5-aminolevulinic acid treatment bear diagnostic implications

Tiffany Hsia<sup>1</sup>  | Anudeep Yekula<sup>1</sup>  | S. Maheen Batool<sup>1</sup>  | Yulia B. Rosenfeld<sup>1</sup> | Dong Gil You<sup>1,2</sup>  | Ralph Weissleder<sup>2,3</sup> | Hakho Lee<sup>2,3</sup> | Bob S. Carter<sup>1</sup> | Leonora Balaj<sup>1</sup> 

<sup>1</sup>Department of Neurosurgery, Massachusetts General Hospital, Harvard Medical School, Boston, Massachusetts, USA

<sup>2</sup>Center for Systems Biology, Massachusetts General Hospital, Boston, Massachusetts, USA

<sup>3</sup>Department of Radiology, Massachusetts General Hospital, Boston, Massachusetts, USA

## Correspondence

Leonora Balaj, Department of Neurosurgery, Massachusetts General Hospital, 185 Cambridge St., Boston, MA, USA  
Email: [balaj.leonora@mgh.harvard.edu](mailto:balaj.leonora@mgh.harvard.edu)

Bob S. Carter, Department of Neurosurgery, Massachusetts General Hospital, 185 Cambridge St. Boston, MA, USA.  
Email: [bcarter@mgh.harvard.edu](mailto:bcarter@mgh.harvard.edu)

Bob S. Carter and Leonora Balaj are co-senior authors.

## Funding information

Division of Cancer Prevention, National Cancer Institute, Grant/Award Numbers: CA069246, CA230697, CA237500, CA239078

## Abstract

Liquid biopsy is a minimally invasive alternative to surgical biopsy, encompassing different analytes including extracellular vesicles (EVs), circulating tumour cells (CTCs), circulating tumour DNA (ctDNA), proteins, and metabolites. EVs are released by virtually all cells, but at a higher rate by faster cycling, malignant cells. They encapsulate cargo native to the originating cell and can thus provide a window into the tumour landscape. EVs are often analysed in bulk which hinders the analysis of rare, tumour-specific EV subpopulations from the large host EV background. Here, we fractionated EV subpopulations in vitro and in vivo and characterized their phenotype and generic cargo. We used 5-aminolevulinic acid (5-ALA) to induce release of endogenously fluorescent tumour-specific EVs (EV<sub>PpIX</sub>). Analysis of five different subpopulations (EV<sub>PpIX</sub>, EV<sub>CD63</sub>, EV<sub>CD9</sub>, EV<sub>EGFR</sub>, EV<sub>CFDA</sub>) from glioblastoma (GBM) cell lines revealed unique transcriptome profiles, with the EV<sub>PpIX</sub> transcriptome demonstrating closer alignment to tumorigenic processes over the other subpopulations. Similarly, isolation of tumour-specific EVs from GBM patient plasma showed enrichment in GBM-associated genes, when compared to bulk EVs from plasma. We propose that fractionation of EV populations facilitates detection and isolation of tumour-specific EVs for disease monitoring.

## KEYWORDS

5-ALA, 5-aminolevulinic acid, extracellular vesicles, glioblastoma, IFC, imaging flow cytometry, nanoFACS, nanoparticle fluorescence activated sorting, PpIX, protoporphyrin IX, liquid biopsy, EV

## 1 | INTRODUCTION

Glioblastoma (GBM) is one of the most aggressive, malignant tumours of the central nervous system (CNS), representing 48.6% of all malignant CNS tumours (Ostrom et al., 2020). As stratified by the WHO CNS5 classification, GBM tumours are grade IV, IDH-wildtype tumours possessing molecular profiles that include mutations to the Telomerase Reverse Transcriptase (TERT) and Epidermal Growth Factor Receptor (EGFR) genes, and demonstrate characteristics of Methylguanine methyltransferase (MGMT) methylation and a combined gain or loss of chromosomes 7/10 (Louis et al., 2021). Highly heterogeneous, the genomic architecture of the tumour complicates treatment design, resulting in poor prognosis (Inda et al., 2014, Sottoriva et al., 2013). The

This is an open access article under the terms of the [Creative Commons Attribution-NonCommercial License](https://creativecommons.org/licenses/by-nc/4.0/), which permits use, distribution and reproduction in any medium, provided the original work is properly cited and is not used for commercial purposes.

© 2022 The Authors. *Journal of Extracellular Vesicles* published by Wiley Periodicals, LLC on behalf of the International Society for Extracellular Vesicles.

current diagnostic standards incorporate a combination of pre-operative visualization and tumour detection via gadolinium contrast-based magnetic resonance imaging (MRI) as well as tissue biopsy for elucidation of molecular pathology (Weller et al., 2021). 5-Aminolevulinic acid (5-ALA; Gliolan) was approved in 2017 as a tool to enhance tumour resection in glioblastoma (Hadjipanayis & Stummer, 2019). Administration of exogenous 5-ALA results in the highly sensitive and specific accumulation of the fluorescent metabolite, protoporphyrin IX (PpIX), in GBM tumour cells over healthy cells. While tissue biopsy provides significant clarity regarding the nature of the disease, even minimally invasive surgical procedures such as stereotactic biopsies are not without complications. Therefore, alternative diagnostic methods of biological fluid components (“liquid biopsies”) have received much interest (Shankar et al., 2017).

A number of different biofluids including whole blood, plasma, cerebral spinal fluid, and saliva have been used to measure different analytes (single circulating tumour cells (CTC), cell clusters, extracellular vesicles (EV), circulating tumour DNA (ctDNA), proteins, metabolites) (Domínguez-Vigil et al., 2018). EVs are a diverse population of nanosized, membrane-bound vesicles, with a variety of ontogenies, that are released into the extracellular space (Beer & Wehman, 2017). Containing cargo reflective of the cell of origin, EVs are able to mediate intercellular communication and can be used to detect tumours, monitor progression or track treatment response. The encapsulated cargo includes DNA and RNA fragments, proteins, and cytosolic molecules (Ghaemmaghami et al., 2020, Roy et al., 2019, Shankar et al., 2017, Skog et al., 2008, Tricarico et al., 2017, Zaborowski et al., 2015). Given the highly vascularized nature of GBM tumours (Das & Marsden, 2013), the release of EVs into the bloodstream allows for measurement of GBM relevant biomarkers including mutations.

Most EV studies to date employ bulk EV analysis from biofluids for mutation detection (Chen et al., 2013, Figueroa & Carter, 2018, Lane et al., 2019). This method of study quantifies both tumour cell-derived (tEV) and host cell-derived EVs (hEV) (Yuana et al., 2013). While the tumour microenvironment has been shown to induce tEV release in biofluids (O’Neill et al., 2019), they are still vastly outnumbered by hEVs. As such, current methods of bulk EV analysis are inherently of lower diagnostic accuracy. Recently, we have successfully characterized a subpopulation of tEVs in the plasma of malignant glioma patients following 5-ALA administration (Jones et al., 2019). 5-ALA is a metabolic precursor of protoporphyrin IX (PpIX), a fluorescent porphyrin that accumulates in cancer cells, and their derived EVs (Maas et al., 2020), upon exogenous dosing. PpIX accumulation can be attributed to several conditions that are intrinsic to the tumour including low ferrochelatase (FECH) activity (Ishizuka et al., 2011) and dysregulation of the Ras/MEK pathway (Chelakkot et al., 2020). Exploitation of these tumour properties can enable sorting and further characterization of tumour EVs.

Improving understanding of the heterogeneous tumour EV landscape will empower tumour-specific, EV-based liquid biopsy studies and downstream clinical translation. Here, we have developed methods for single EV phenotype-based analysis, EV subpopulation isolation, and characterized the RNA cargo from five GBM-derived EV subpopulations. We have identified, quantified, and validated a tumour-specific subpopulation of EVs that, when isolated, shows enrichment of tumour signal in standard PCR assays.

## 2 | METHODS

### 2.1 | Cell lines

Human glioma cell lines expressing EGFR wild type or constitutively active mutant epidermal growth factor receptor (Gli36<sup>EGFRwt</sup>, Gli36<sup>EGFRvIII</sup>; RRID:CVCL\_RL88) were cultured in Dulbecco’s Modified Eagle Medium (DMEM; Invitrogen, Waltham, MA) with high glucose containing 10% foetal bovine serum (FBS; Life Technologies Corporation, Carlsbad, CA, USA) and 1% Penicillin/Streptomycin Solution (Pen/Strep; Life Technologies Corporation, Carlsbad, CA, USA). Gli36 cell lines were generated at Massachusetts General Hospital with approved IRB procedures. The expression of EGFRvIII was confirmed using droplet digital PCR (ddPCR; see section 2.1). The human U87 Malignant Glioma (ATCC HTB-14; RRID:CVCL\_0022) cell line was cultured in high glucose DMEM containing 10% FBS and 1% Pen/Strep. All experiments were performed at a cell confluency of 70%–80% to minimize cell death. Mycoplasma contamination was tested monthly using a commercial mycoplasma PCR kit (PCR Mycoplasma Detection kit; Applied Biological Materials Incorporated, BC, Canada).

### 2.2 | Cell line 5-ALA dosing

5-ALA (Sigma-Aldrich, St. Louis, MO, USA) was reconstituted to 2.9 M in sterile 0.22  $\mu\text{m}$  filtered 1X phosphate buffered saline (PBS; ThermoFisher Scientific, Waltham, MA, USA) and stored at  $-20^{\circ}\text{C}$ . On day 0, all three cell lines were plated at a density of 1 million cells on 100 mm diameter plates (Nunc EasYDish; Thermo Fisher Scientific, Waltham, MA) in 10 ml of media. On day 1, the media was replaced with EV-free media: DMEM, containing 3% EV-depleted foetal bovine serum (EV-free FBS; Life Technologies Corporation, Carlsbad, CA, USA) and 1% Pen/Strep. The cells were also dosed with a final concentration of 0.8 mM 5-ALA or mock-dosed with 1X PBS of the same volume, according to a previously identified optimal in vitro dosage (Jones et al.,

2019). On day 2, conditioned media was collected for analysis and processed as described below. All the experiments were performed in a dark room, with the plates and conical tubes always covered with aluminium foil to minimize PpIX photobleaching as previously established (Jones et al., 2019). Cell viability, maintained at 80% and above, was assessed using the Countess II FL Automated Cell Counter (ThermoFisher Scientific, Waltham, MA, USA).

### 2.3 | Conditioned Media (CM) processing

The media collected from 5-ALA or mock dosed cells was centrifuged at  $300 \times g$  for 5 min at room temperature (RT) to remove floating cells. The supernatant was collected and centrifuged again at  $2000 \times g$  for 20 min at RT and filtered using a  $0.8 \mu\text{m}$  filter to remove cellular debris and other aggregates. The media was stored in amber tubes at  $-80^\circ\text{C}$  until further analysis. This processed media is henceforth referred to as “conditioned media.”

### 2.4 | Tumour tissue processing

Tumour tissue was collected immediately following surgical resection, flash frozen in RNAlater Stabilization solution (Invitrogen, Waltham, MA, USA), and stored at  $-80^\circ\text{C}$ .

### 2.5 | Blood plasma processing

Whole blood was collected in K2 EDTA tubes containing an inert gel barrier (BD Vacutainer, Franklin Lakes, NJ, USA) and processed within 2 h of collection. Samples were centrifuged for 10 min at  $1100 \times g$  at  $20^\circ\text{C}$  and slowly passed through a  $0.8 \mu\text{m}$  filter. Plasma was aliquoted into 1 ml volumes and stored at  $-80^\circ\text{C}$ . Patient samples were collected 3 h following 5-ALA administration and were processed with minimized light exposure.

### 2.6 | Ethics approval and consent to participate

All participants were briefed, and written, informed consent was obtained. The study was approved by the Institutional Review Board (IRB) ethics committee at the Massachusetts General Hospital.

### 2.7 | EV labelling

Whole conditioned media, from Section 2.3, was taken directly for intact EV labelling. Conditioned media was aliquoted into  $100 \mu\text{l}$  aliquots in replicates of 3 for each labelling condition ( $n = 3$ ). For antibody labelling, EVs were first blocked using Human TruStain FcX (BioLegend, San Diego, CA, USA) for 10 min at RT. PE-conjugated anti-human antibody was added according to the optimized volumes. The anti-human CD63 antibody (Clone H5C6; BioLegend, San Diego, CA, USA), anti-human CD9 antibody (Clone HI9a; BioLegend, San Diego, CA, USA), and anti-human EGFR (Clone AY13; BioLegend, San Diego, CA, USA) antibodies were used for this study. IgG controls were performed using the PE-conjugated anti-human IgG Fc (Clone M1310G05; BioLegend, San Diego, CA, USA). CFDA-SE labelling was performed using a 1:100 dilution of 10 mM CFDA-SE (CFDA; Invitrogen, Waltham, MA) in dimethyl sulfoxide (DMSO; Sigma Aldrich, St. Louis, MO). Following labelling, unbound antibody and dye was eliminated via 100 kDa centrifugation filtration. The final sample was restored to  $100 \mu\text{l}$  using  $0.22 \mu\text{m}$  filtered 1X PBS.

### 2.8 | ImageStream analysis

ImageStreamX (ISX) MkII Imaging flow cytometer (IFC; Amnis Corporation, Seattle, WA) was used for analysis of fluorescent EVs as previously described (Jones et al., 2019). SPIRE version 200.1.620.0 instrument software was used for instrument setup, calibration, and data acquisition. Channels Ch 01 and Ch 09 were set to brightfield to permit spatial coordination between cameras. Channel 06 was set to side scatter. Analysis was performed with fluidics set at low speed, high sensitivity,  $60\times$  magnification, and a core size of  $7 \mu\text{m}$ . The “Hide Beads” option was unchecked prior to each acquisition in order to visualize speed beads in analyses. All parameters are stored in the acquisition template, except the latter, which requires unchecking prior to each acquisition. The appropriate lasers (CFDA: 488 nm; PE: 561 nm; and PpIX: 642 nm; 120 mW) were run at maximal power to ensure

maximal sensitivity. To avoid the risk of co-incident particle detection, EV samples were run at concentrations lower than 1010 objects/ml. Acquisition was performed at a constant Flow Speed, ensuring that Flow Speed Error CV was maintained under 0.2. Instrument priming was performed when the Flow Speed became unstable. Samples were allowed to run for 1–2 min prior to acquisition, to reach a stable Flow Speed and a low Flow Speed Error CV. IDEAS data analysis software was used for data analysis.

The following gates were generated for EV quantification. The R0 collection gate (white), which plots fluorescence intensity (Ch 11) versus side scatter (Ch 06), was set to exclude the majority speed bead events. The events within the R0 gate were collected for further analysis. RIF files were generated, merged, compensated, and a gating strategy was used for consistency. A uniform gating strategy was applied: (1) all fluorescent events were plotted against the side scatter (Ch06), (2) all events that showed low SSC (<500) but a fluorescent intensity were used for further analysis (>10,000 events were acquired), (3) Inspire masking was used for Ch01 and Ch09 to detect any events that showed a brightfield image, (4) a new feature was created by using the Raw Max Pixel feature on the created inspire mask for Ch01 and Ch09 to exclude any events that had a brightfield image, (5) Inspire masking was used to detect any fluorescent image in the recorded channels (Ch02, Ch03, Ch07, and Ch11), (6) swarm detection was excluded by using the spot counting feature on the inspire mask for Ch02, Ch03, Ch07 and Ch11 and by eliminating any events that showed more than 1 spot, and (7) all remaining events were labelled as single EVs and analysed for their multiparameter signals. An example of the gating strategy can be found in Figure S1F.

## 2.9 | Astrios NanoFacs

EVs were labelled as described above and sorted using the MoFlo Astrios EQ, Cell Sorter (Beckman Coulter, Brea, CA, USA). 100,000 fluorescent EVs from cell lines and 250,000 fluorescent EVs from patient samples were sorted into 200  $\mu$ l of sterile, filtered 1 $\times$  PBS for downstream analysis. QC was performed according to manufacturer's recommendations. All instrumentation and protocols were configured for small particle detection. Due to the MoFlo Astrios EQ's alignment system, micrometres on the FSC attachments were adjusted daily to maximize forward scatter (FSC) signalling. The beam splitter was removed from the FSC assembly to maximize the amount of laser light detected through the FSC1 photomultiplier tube (PMT) detector. The Beckman Coulter MoFlo AstriosEq is equipped with two FSC PMT pathways separated by a beam splitter (60/40 split). FSC1 is a direct laser beam pathway (60) and the FSC2 is directed at an angle from the beam splitter (40). Following removal of the beam splitter, 100% of laser light was directed to the FSC1 pathway. Seven different and unique masks were generated to optimize particle identification and focus laser light to the PMTs. After testing all the masks, the P1 mask was chosen for small particle detection, as the larger opening maximizes resolution and dynamic range. Finally, 561 nm side scatter (SSC) was assigned as the Trigger parameter and FSCA Log versus SSCA Log was plotted for population determination. We ensured the ability to trigger from any of the scatter parameters associated with the six collimated laser lines. The 561 nm SSC was chosen due to its location at the centre of the seven pinholes. Testing of the remaining five SSC parameters was performed and similar results were recorded. NIST-traceable beads were diluted to a concentration of  $1 \times 10^5$  beads/ml to minimize coincidence detection (Table S5). Instrument voltages were adjusted so that all bead sizes were visible within the 561 SSC channel and each bead was acquired until a minimum of 10,000 events were recorded. The primary gating threshold was set below the 100 nm bead population.

Conditioned media was used to determine background noise without sample contribution. A combination of the conditioned media and NIST beads were used to determine gating strategy. Sample fluorescence was read in the 405–620/29 channel for EV<sub>PPIX</sub>, 488–513/26 channel for the CFDA, and 561–579/16 channel for the CD9, CD63, and EGFR. The drop drive frequency was maintained at approximately 90 kHz with the plate voltage and amplitude set to 3500 and 15 volts, respectively. Samples were sorted in purity mode until 100,000 events were collected. All nanoflow setup was conducted according to previously established methods (De Oliveira et al., 2020, Welsh et al., 2020).

## 2.10 | Nanoparticle tracking analysis (NTA)

NTA measurements were obtained using the NanoSight NTA (LM10; Malvern Panalytical, Malvern, United Kingdom) at a 20 $\times$  magnification with a scientific CMOS camera and blue (405 nm) laser module. Samples were injected into the sample chamber and imaging was obtained over the course of 30 s. Two replicates were repeated for each sample ( $n = 2$ ). NTA v3.1 software was used for analysis and the detection threshold was manually adjusted between 4 and 5 depending on varying levels of background noise. The instrument chamber was thoroughly cleaned with distilled water followed by  $\geq 80\%$  ethanol (Fisher Scientific, Waltham, MA, USA) between each sample. All measurements were normalized to DMEM + 3% EV-free FBS + 1% PS or RPMI + 3% EV-free FBS + 1% PS, respectively. Size distribution data obtained from all replicates were compiled using MATLAB.

## 2.11 | Droplet digital PCR

Following RNA extraction, cDNA was prepared according to the SuperScript VILO cDNA Synthesis kit protocol (ThermoFisher Scientific, Waltham, MA, USA). 2  $\mu$ l of prepared cDNA was used in ddPCR amplification. Assays for *GREM1*-FAM (*GREM1*: Hs01879841\_s1) and *GAPDH*-VIC (*GAPDH*: Hs99999905\_m1) were obtained through ThermoFisher Scientific (Waltham, MA, USA). In addition to the cDNA template, ddPCR amplification was performed using 10  $\mu$ l of 1X ddPCR Supermix for probes (no dUTP; Bio-Rad, Hercules, CA, USA), 1  $\mu$ l of *GREM1*-FAM assay, 1  $\mu$ l of *GAPDH*-VIC assay, and 6  $\mu$ l UltraPure Distilled H<sub>2</sub>O (Invitrogen, Waltham, MA, USA) for a total reaction volume of 20  $\mu$ l. Droplet Generation Oil for Probes (Bio-Rad, Hercules, CA, USA) and the QX200 manual droplet generator (Bio-Rad, Hercules, CA, USA) were subsequently used to generate droplets. The thermocycling conditions used are as follows: Stage 1 was cycled one time with a ramp rate of 51% up to 95°C and held for 10 min; Stage 2 consisted of 40 cycles of a 94°C (51% ramp rate) hold 30 s followed by a 1 min hold at 60°C (51% ramp); and the final stage was a 10 min hold at 98°C (51% ramp rate) prior to an infinite hold at 4°C (20% ramp rate). The plate was held at 4°C for 15 min before transfer to the droplet reader. Droplet counts were taken using the QX200 droplet reader (Bio-Rad, Hercules, CA, USA) and analysis conducted via QuantaSoft version 1.7.4 (Bio-Rad, Hercules, CA, USA).

## 2.12 | Extraction of RNA from tumour

Tumour tissue was thawed on ice from -80°C and RNA extraction was performed using the RNeasy kit (Qiagen, Hilden, Germany) following the recommended protocol.

## 2.13 | Extraction of RNA from plasma

1 ml of plasma was thawed at room temperature from -80°C. RNA was extracted using the exoRNeasy kit (Qiagen, Hilden, Germany) per manufacturer's instructions. All eluted RNA was used for downstream applications.

## 2.14 | Extraction of RNA from sorted EVs

EV suspension volume following nanoFACS sorting was approximated and Qiazol (from the exoRNeasy kit) and chloroform (ThermoFisher Scientific, Waltham, MA, USA) volumes were adjusted according to a 15  $\mu$ l:70  $\mu$ l:9  $\mu$ l ratio (EV suspension:Qiazol:chloroform). Qiazol was added to the tube, the tube inverted several times, and briefly vortexed to ensure thorough mixing. The solution was incubated at room temperature for 10 min. The previously determined volume of chloroform was added to the tube and the solution was vigorously shaken for 15 s. From here, the exoRNeasy protocol was followed, picking up from step 10 (3 min chloroform/phenol incubation).

## 2.15 | Library preparation

Complementary DNA (cDNA) libraries were prepared from RNA according to the protocols recommended by the QIAseq UPX 3' Transcriptome Kits (Qiagen, Hilden, Germany). Quality control measures were conducted using the StepOne Real-Time PCR System (ThermoFisher Scientific, Waltham, MA, USA) and High Sensitivity DNA assay via the 2100 BioAnalyzer Instrument (Agilent Technologies, Santa Clara, CA, USA). PCR conditions followed those described in the QIAseq UPX 3' Transcriptome protocol.

## 2.16 | MiSeq sequencing

Libraries were diluted to 4 nM using UltraPure Distilled H<sub>2</sub>O (Invitrogen, Waltham, MA, USA) and pooled at equal volumes. A PhIX library was also prepared at 4 nM. Based on the BioAnalyzer results of the prepared libraries, a 4 nM concentration was approximately equated to a Qubit 4 Fluorometer (ThermoFisher Scientific, Waltham, MA, USA) reading of 1.4 ng/ $\mu$ l. Both libraries were denatured using 0.2 N NaOH for 5 min and quenched with ice cold HT1 buffer from the MiSeq Reagent Kit v3 (Illumina, San Diego, CA, USA). A final library pool was prepared with 540  $\mu$ l of denatured pooled library and 60  $\mu$ l of denatured PhIX library. The thawed cartridge was prepared and the sample was loaded according to the manufacturer's instructions. The MiSeq instrument was prepared, as prompted by the software, for run initiation.

## 2.17 | Data analysis

Primary analysis of the files generated by MiSeq was conducted using Qiagen GeneGlobe. Subsequent FASTQ files were demultiplexed and further analysed using Qiagen CLC Workbench. The analysis pipeline on CLC Workbench consists of five steps: (1) annotation of Unique Molecular Indices (UMI), (2) adapter trimming from ligated sequences, (3) generation of UMI reads, (4) removal of low quality and ambiguous reads, and (5) RNA-seq analysis as mapped to the human genome (GRCh37.p12). All differential expression (DE) analysis utilized TMM normalization and graphs were produced using CLC Workbench. Gene ontology was performed with the aid of [metascape.org](http://metascape.org) (Zhou et al., 2019). Further analysis was conducted in R and MATLAB. Kaplan-Meier curves for GBM samples, stratified by high and low expression, were generated using the REpository of Molecular BRAin Neoplasia DaTa (REMBRANDT) as accessed through [betastasis.com](http://betastasis.com). Analysis was performed using the Affymetrix HT HG U133A platform.

## 3 | RESULTS

### 3.1 | Characterization of cells and EVs following 5-ALA dosing

To investigate the influence of 5-aminolevulinic acid (5-ALA) on cells and EVs, three human GBM cell lines (Gli36<sup>EGFR<sup>III</sup></sup>, Gli36<sup>EGFR<sup>wt</sup></sup>, and U87) were dosed with 5-ALA and the total concentration (Figure 1A) and size distribution (Figure 1B) of released EVs were quantified using Nanoparticle Tracking Analysis (NTA). We observed cell line-specific EV production with no significant differences in bulk EV concentrations following 5-ALA dosing. Additionally, EV size distributions across the three cell lines were maintained following dosing. Following bulk EV characterization, we stratified total EVs into subpopulations, optimizing in vitro fluorescent labelling of four EV subpopulations: epidermal growth factor receptor (EGFR; henceforth EV<sub>EGFR</sub>), the common EV tetraspanin markers (CD63, CD9; EV<sub>CD63</sub>, EV<sub>CD9</sub>), and an esterase dependent marker (carboxyfluorescein diacetate succinimidyl ester, CFDA; EV<sub>CFDA</sub>). Based on Minimal Information for Studies of Extracellular Vesicles (MISEV) (Théry et al., 2018) guidelines, we incorporated a range of controls, including lysis controls, in our optimization to delineate true positive events to establish reproducible labelling and gating methods (see Section 2.8 and Figure S1). Using single EV analysis, EV subpopulations were evaluated before and after 5-ALA dosing, finding that the majority of EV subpopulations remained unaltered. We noted a statistically significant decrease in EV<sub>CD63</sub> and EV<sub>CD9</sub> release from U87 cells ( $p = 0.0018$  and  $p = 0.0008$ , respectively) and an increase in EV<sub>CD63</sub> from the Gli36<sup>EGFR<sup>wt</sup></sup> cell line ( $p = 0.0004$ ; Figure 1C). However, no significant difference in mean EV<sub>CFDA</sub>, EV<sub>CD63</sub>, EV<sub>CD9</sub>, and EV<sub>EGFR</sub> fluorescence intensity was observed before and after 5-ALA dosing across the three cell lines (Figure S2). Previously, we have shown the production of a fluorescent subpopulation of EVs (EV<sub>PpIX</sub>) following 5-ALA dosing (Jones et al., 2019). With this additional subpopulation, we now compare cell line-specific subpopulation prevalence and production following 5-ALA dosing across the three different GBM cell lines. We identified a broad range of subpopulation production and release with EV<sub>CFDA</sub> prevalence being the highest ( $1.5 \times 10^7$ – $3.1 \times 10^7$  EVs/ml), followed by EV<sub>CD9</sub> ( $2.9 \times 10^6$ – $6.7 \times 10^6$  EVs/ml), EV<sub>CD63</sub> ( $3.2 \times 10^5$ – $6.4 \times 10^5$  EVs/ml), EV<sub>EGFR</sub> ( $2.6 \times 10^5$ – $3.4 \times 10^5$  EVs/ml), and EV<sub>PpIX</sub> ( $1.4 \times 10^3$ – $2.3 \times 10^4$  EVs/ml; Figure 1D). Importantly, however, the relative prevalence of the EV subpopulations was retained across cell lines. In congruence with the CFDA labelling mechanism, fluorescent activity following reactivity with intra-EV lysine residues and amine sources, CFDA-positive EV production exceeds that of tetraspanin- and PpIX-positive EVs.

Following 5-ALA dosing, we determined a significant increase in the mean cell (Figure 1E) and EV<sub>PpIX</sub> fluorescence (Figure 1F), with no fluorescent EVs detected in mock-dosed cells. As a result of 5-ALA dosing, EV<sub>PpIX</sub> were produced at the following concentrations by Gli36<sup>EGFR<sup>III</sup></sup>, Gli36<sup>EGFR<sup>wt</sup></sup>, and U87 cells:  $7.5 \times 10^3 \pm 1.9 \times 10^3$  EVs/ml,  $1.4 \times 10^3 \pm 8.8 \times 10^2$  EVs/ml, and  $2.4 \times 10^4 \pm 4.4 \times 10^3$  EVs/ml, respectively (Figure 1G). Interestingly, the mean cell fluorescence did not correlate with the mean EV fluorescence ( $r^2 = 0.27$ ; Figure 1H), despite high correlation with the number of EV<sub>PpIX</sub> (expressed in percent of total as determined by NTA) released by the three cell lines ( $r^2 = 0.84$ ; Figure 1I). We also determined a strong positive correlation between EV size and EV<sub>PpIX</sub> fluorescence ( $r^2 = 0.89$ ; Figure 1J).

### 3.2 | RNA sequencing of EV subpopulations reveals their unique genetic cargo

We first established a robust workflow for fluorescence-based sorting of EVs (nanoFACS) from conditioned media based on MISEV guidelines (see Section 2 and Figure S3). Beads (individual sizes and as a mix) and medium controls (conditioned media and IX PBS alone or spiked with fluorescent liposomes) were tested to establish background interference and fluorescence threshold (Figure S4). Using this protocol, 100,000 fluorescently-labelled EVs of each subpopulation were sorted from each cell line. Sorted EVs were then lysed using an adjusted exoRNeasy (Qiagen) EV RNA extraction protocol, as described in Section 2.

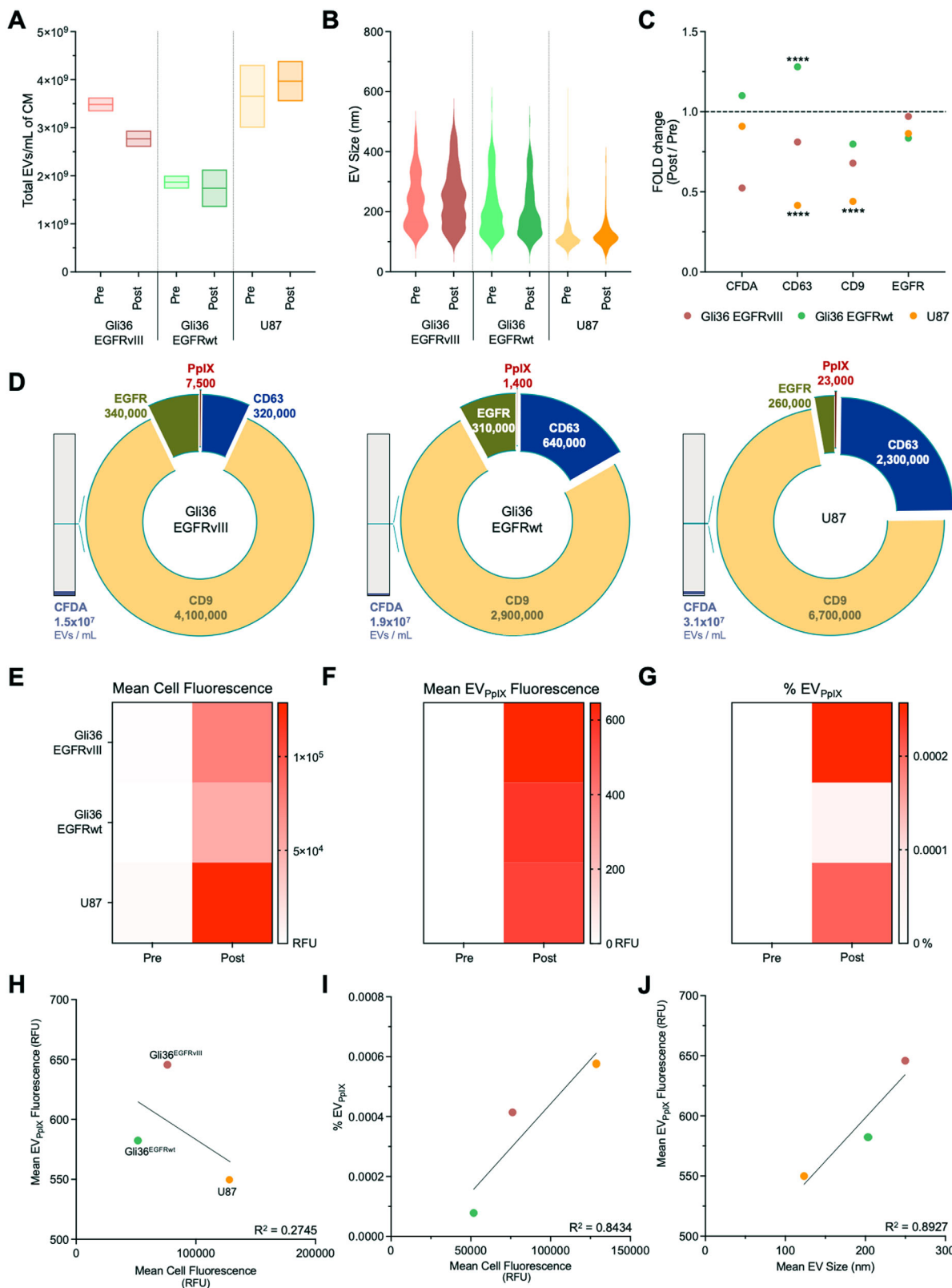


**FIGURE 1** Effects of 5-aminolevulinic acid (5-ALA) dosing on EV subpopulations. GBM cell lines were dosed with 5-ALA and the released EVs were analyzed pre-5-ALA and post-5-ALA dosing. Biological replicates ( $n = 2$ ) and technical replicates ( $n = 3$ ) per each biological replicate (total  $n = 6$ ) were utilized for each analysis. The total number (A) and size distribution of EVs (B) was determined using NTA. Comparison of EV concentration between pre- and post-5-ALA showed  $p$ -values of 0.37, 0.99, and 0.87 for Gli36<sup>EGFRvIII</sup>, Gli36<sup>EGFRwt</sup>, and U87, respectively. EVs from 5-ALA dosed GBM cells pre- and post-5-ALA dosing were stained with CFDA-SE and phycoerythrin-conjugated antibodies (CD63, CD9, EGFR). All EV subpopulations including EV<sub>PpIX</sub> were studied using IFC. Average positive events are described by EVs/ml of conditioned media. Relative fold changes of each EV subpopulation pre- and post-5-ALA dosing were determined and calculated for significance (C; Gli36<sup>EGFRwt</sup> EV<sub>CD63</sub>:  $p = 0.03$ ; U87 EV<sub>CD63</sub>:  $p = 0.002$ ; U87 EV<sub>CD9</sub>:  $p = 0.0008$ ).

(Continues)

FIGURE 1 (Continued)

Relative subfractions of EV subpopulations following 5-ALA dosing (as quantified by IFC) represented as a fraction of total EVs (gray, measured by NTA) were analyzed for abundance (D): EV<sub>CFDA</sub> (purple), EV<sub>CD63</sub> (dark blue), EV<sub>CD9</sub> (yellow), EV<sub>EGFR</sub> (green), and EV<sub>PpIX</sub> (red). The mean cell fluorescence of GBM cells pre- and post-5-ALA dosing (E), the mean EV<sub>PpIX</sub> fluorescence (F) and the relative fraction of EV<sub>PpIX</sub> from the NTA-derived total (G), were plotted to compare relative fluorescence and abundance. Correlative analysis of mean cell PpIX fluorescence and mean EV<sub>PpIX</sub> fluorescence (H), mean cell PpIX fluorescence against relative fraction of EV<sub>PpIX</sub> (I), and mean EV size against mean EV PpIX fluorescence (J) was performed.

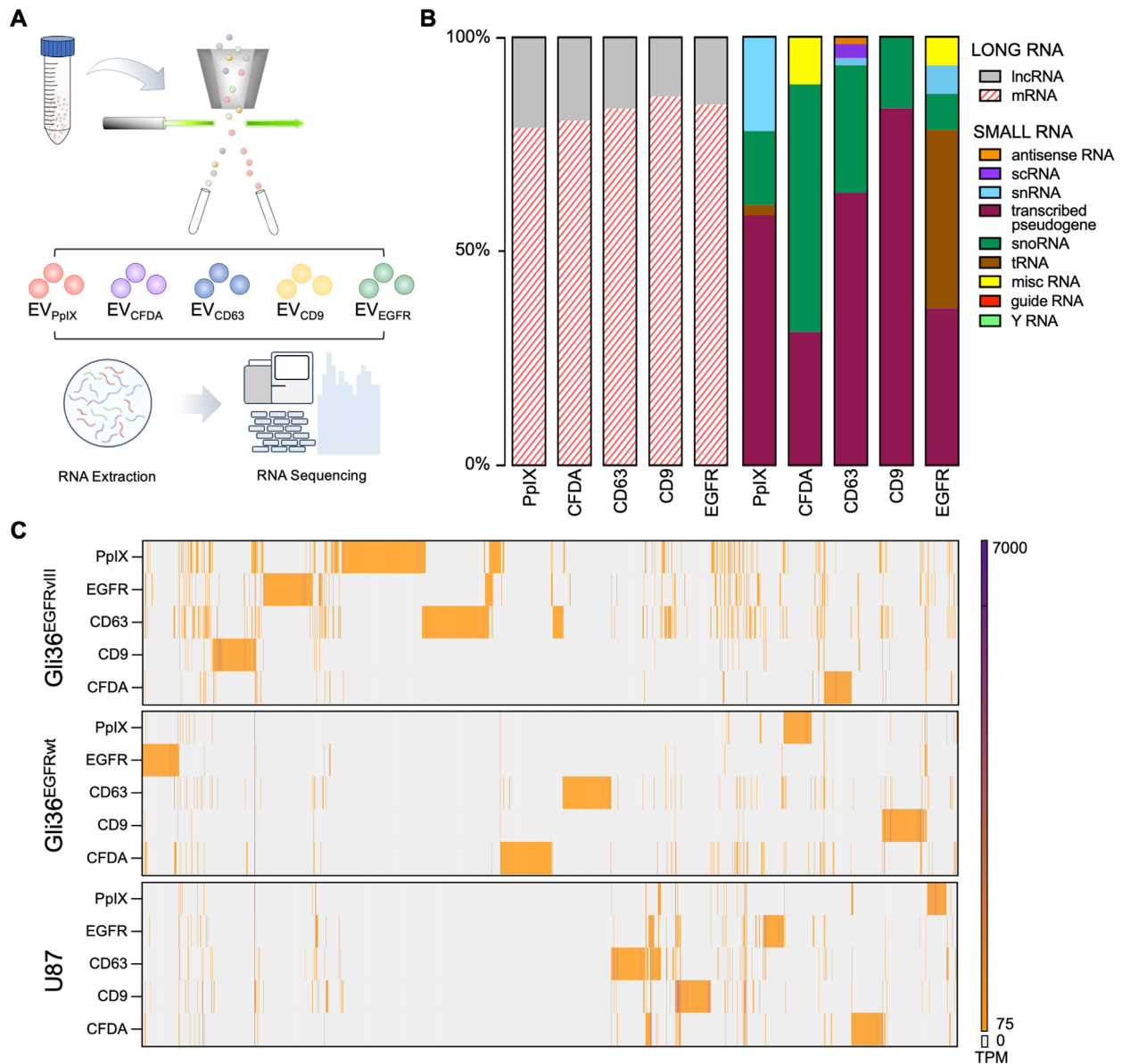


**FIGURE 2** Quantification of cell line-derived EV subpopulation cargo. EVs were fluorescently labeled and sorted using nanoFACS. A workflow for EV sorting and downstream library preparation was developed for low-input, bulk RNA sequencing (A). The relative RNA landscape of EV subpopulations as defined by long and small RNA biotypes was mapped according to detection (B). Gene expression (transcripts per million; TPM) across EV subpopulations and cell lines were assessed in order of phylogenetic relation (C).

The resulting RNA was quantified for quality control and multiplexed libraries were prepared for sequencing using UPX whole transcriptome, which enriches for poly-adenylated RNAs (Figure S5A, Figure 2A).

First, we sought to determine whether 5-ALA led to any differences in EV RNA cargo, by analysing total conditioned media which includes all EV subtypes. Differential expression analysis of the total EV transcriptome across three cell lines revealed no significant difference in gene expression upon 5-ALA dosing (Figure S5B–D). We then proceeded with sequencing all five subpopulations from three GBM cell lines following 5-ALA dosing.

**TABLE 1** Average RNA landscape of glioblastoma derived EVs

	PpIX	CFDA	CD63	CD9	EGFR
~1 count/100k EVs		misc. RNA	antisense RNA scRNA snRNA	snoRNA	misc. RNA snRNA snoRNA tRNA
>1 count/100k EVs	snRNA snoRNA tRNA pseudogene	snoRNA pseudogene	snoRNA pseudogene	pseudogene	pseudogene
>1 count/10k EVs	lncRNA	lncRNA	lncRNA	lncRNA	lncRNA
>1 count/1k EVs	mRNA	mRNA	mRNA	mRNA	mRNA

We first determined the total number of each RNA species for each EV subpopulation and divided that by 100,000 EVs (total number of sorted EVs). Our analysis shows >1 count of mRNA/1000 EVs (messenger RNA, mRNA), followed by lncRNA at >1 count/10,000 EVs (long non-coding RNA, lncRNA), and  $\geq 1$  count/100,000 EVs of small RNAs (Table 1). Average relative comparison of long RNA (transcripts larger than 100 nt) and small RNA populations (Wei et al., 2017) reveals a predominance of mRNAs in all EVs and unique small RNA profiles within each subpopulation (Figure 2B). Uniquely, we identify elevated levels of lncRNAs in the EV<sub>PpIX</sub> population and a decreased diversity in small RNA populations, encompassing only small nuclear RNA (snRNA), small nucleolar RNA (snoRNA), transcribed pseudogenes, and a small population of transfer RNAs (tRNA). These subpopulation-unique landscapes are similarly reflected in the genetic expression. Through phylogenetic mapping of genetic expression in each subpopulation, we likewise identified discrete regions of enrichment unique to each EV subpopulation of each cell line (Figure 2C). Further analysis of individual subpopulations demonstrated expression of RAS pathway genes, namely Kirsten rat sarcoma viral oncogene homolog (*KRAS*) and proto-oncogene B-Raf and v-Raf murine sarcoma viral oncogene homolog B (*BRAF*), packaging into the Gli36<sup>EGFR<sup>vIII</sup></sup>-derived EV<sub>PpIX</sub> population, which warrants further exploration.

Further comparative mapping of gene expression from subpopulations derived from a common cell line show, on average, four common genes across all five subpopulations (Figure 3A). Furthermore, we conducted a series of characterized and uncharacterized mRNAs and lncRNAs of varying expression levels that we redefined as unique to each EV subpopulation, and common across cell lines (Figure 3B). Notably, *Gremlin1* (*GREM1*) and *LOC105379070*, are found to maintain similar expression levels across the various subpopulations. Statistical variation due to cell lines and subpopulations was non-significant (*GREM1*:  $p = 0.8242$  and  $0.8552$ ; *LOC105379070*:  $p = 0.5959$  and  $0.8517$ , respectively). Notably, we perceive the highest number of common genes within the CD63 subpopulation, suggesting a more global biogenetic pathway than other subpopulations. We further assess enrichment of the total EV transcriptome with respect to EV subpopulations, which has revealed distinct, phylogenetically similar regions of elevated detection within each cell line (Gli36<sup>EGFR<sup>vIII</sup></sup>, Gli36<sup>EGFR<sup>wt</sup></sup>, and U87) and each subpopulation. Ontological analysis of these regions and isolation of statistically significant pathways show unique process enrichment for each subpopulation. We found the region of interest in EV<sub>PpIX</sub> to involve cellular migratory and meiotic and nucleic acid regulatory processes across all three cell lines, with different cellular origins influencing pathway enrichment (Figure S6, Table S1). Furthermore, regions identified in the EV<sub>CD63</sub> and EV<sub>CD9</sub> populations in all three cell lines enriched for pathways regulating cytoskeleton organization, cell cycle, and growth. Interestingly, the regions identified in total conditioned media consistently regulate the cellular life cycle, including a variety of biosynthetic processes, cell and nuclear division, and organelle organization. This comparison of isolated EV subpopulations against total EVs derived only from GBM cells (in vitro) reveals the distinct potential for specific gene enrichment following EV isolation.

Each subpopulation transcriptome was then aligned to the KEGG orthology (KO) database and all significantly represented pathways were evaluated for their role in GBM development and progression (Figure 3C; Table S2). Of the significant KO represented pathways identified, EV<sub>PpIX</sub> demonstrate the highest alignment to cancer-affiliated pathways as compared to the other EV subpopulations (EV<sub>PpIX</sub>: 78.26%, EV<sub>CFDA</sub>: 42.86%, EV<sub>CD63</sub>: 48.00%, EV<sub>CD9</sub>: 43.75%, EV<sub>EGFR</sub>: 66.67%).

### 3.3 | Patient-derived EV<sub>PpIX</sub> enrich for tumour specific cargo

Following the EV isolation pipeline established in cell lines, PpIX-fluorescent EVs were isolated from the plasma of GBM patients undergoing 5-ALA fluorescence guided surgery. Matched tissue and total EVs from plasma samples were also collected for processing and bulk RNA sequencing (Figure 4A). Similar to the bulk EV processing we implemented for the in vitro study, total EV populations were isolated and processed from plasma using exoRNeasy.

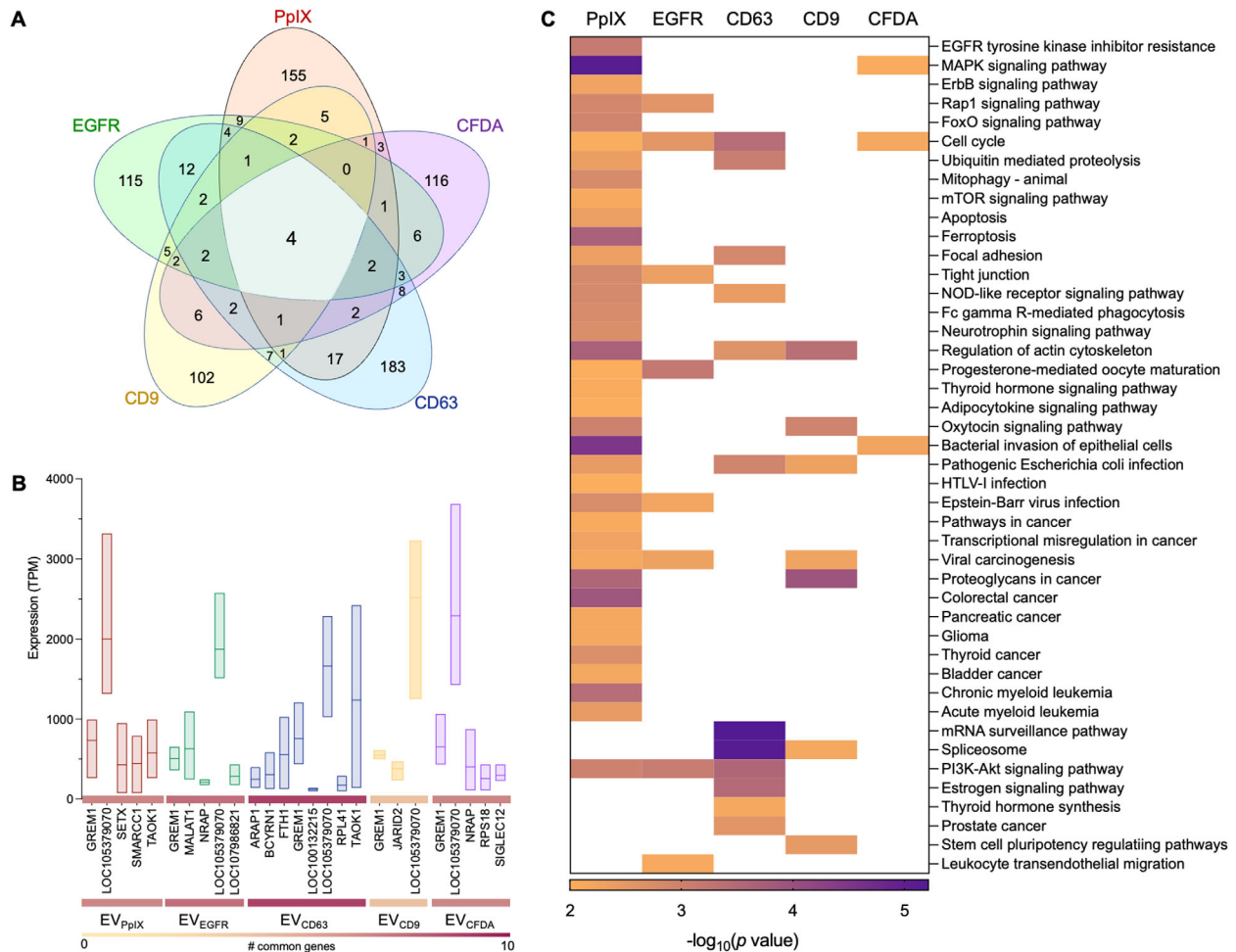


**FIGURE 3** Transcriptomic commonalities across cell line-derived EV subpopulations. Comparative analysis was performed to determine the average number of common genes among subpopulations (A) and within subpopulations across cell lines (B). All genes expressed in each subpopulation were analyzed via KEGG orthological analysis and all significant pathways associated with cancer were identified (C). Significance was designated at  $-\log_{10}(p \text{ value}) \geq 2$ .

**TABLE 2** RNA Landscape of patient plasma

	PpIX
~1 count/100k EVs	tRNA
>1 count/100k EVs	pseudogene
>1 count/10k EVs	lncRNA mRNA

The patient cohort represented a variety of GBM molecular profiling including MGMT methylation, EGFR status, Phosphatase and TENsin homolog deleted on chromosome 10 (PTEN) status (Figure 4B). We assessed the RNA landscape of patient derived EV<sub>PpIX</sub> and total EVs from matched patient plasma, calculating the average relative expression from all patients (Figure 4C). In comparison with the GBM cell line derived EV<sub>PpIX</sub> long RNA profile, we observed a similar long RNA profile in EV<sub>PpIX</sub> derived from patient plasma, with a relative lncRNA abundance of 21.2% and 19.1%, respectively. Conversely, lncRNA abundance in total EVs derived from patient plasma averaged 9.0%, demonstrating enrichment following EV<sub>PpIX</sub> isolation. We further quantified the prevalence of the types of RNAs within the patient derived EV<sub>PpIX</sub> population, with mRNA as the most predominant RNA species (Table 2). Following RNA biotype stratification, we compared the total transcriptome expression in sorted EV<sub>PpIX</sub> to that of the genetic cargo found in tumour tissue and total plasma EVs (Figure 4D). It is important to note that expression has been quantified relative to each sample, exhibiting enhanced detection of tumour-derived genes. Interestingly, of the common genes identified in both EV<sub>PpIX</sub> and tumour tissue, only 50.6% of the genes are found expressed in the total EVs derived from plasma. Reactome analysis of total EV<sub>PpIX</sub> cargo revealed enrichment of cancer related pathways, such as oxidative stress induced

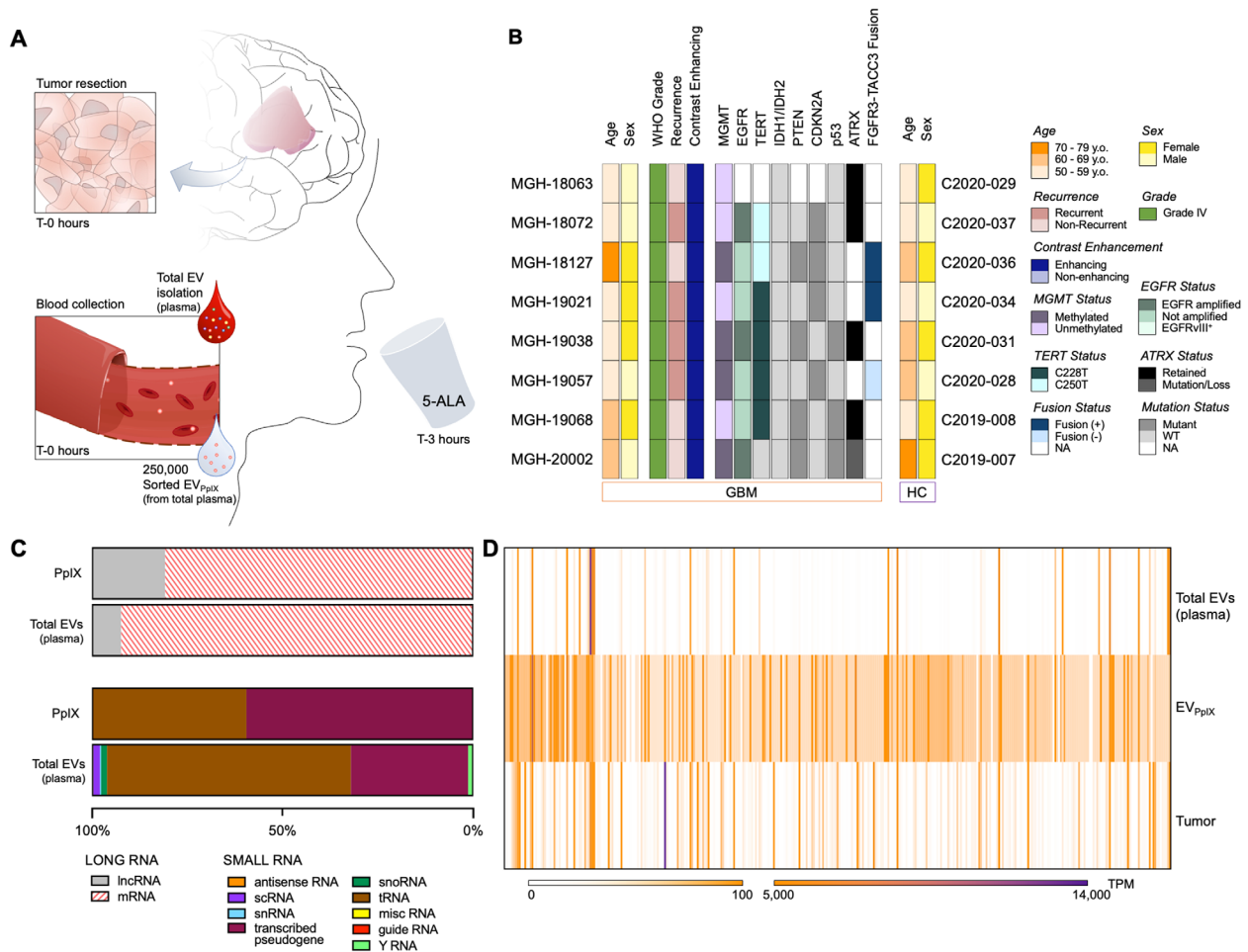


**FIGURE 4** RNA sequencing of matched EV<sub>PpIX</sub>, plasma total EVs, and tumor tissue. A workflow for biological sample collection and the downstream extraction, library preparation, and low-input, bulk RNA sequencing was developed for application in the patient cohort (A). A patient cohort (GBM;  $n = 8$ ) and an age-matched healthy cohort (HC;  $n = 8$ ) was built for sample collection. Both cohorts are composed of an even sex distribution. Patient cohort inclusion parameters consisted of a clinical glioblastoma diagnosis and 5-ALA fluorescence guided surgery (B). The RNA landscape of sorted EV<sub>PpIX</sub> and total EVs derived from plasma was examined and plotted relative to total long RNAs and small RNAs (C). Average patient sample gene expression of the genes detected in the EV<sub>PpIX</sub> transcriptome was calculated and mapped in order of phylogenetic relationship for each biological sample type (D).

senescence, DNA methylation, Notch signalling, Wnt signalling, and amino acid metabolism, as compared to total plasma EVs, which involved pathways associated with systemic processing (e.g., adaptive and cytokine signalling in the immune system, amino acid metabolism, translation initiation; Table S3).

Differential expression analysis (Robinson & Oshlack, 2010) of the healthy plasma EV transcriptome (control) as compared to patient derived EV<sub>PpIX</sub> demonstrates downregulation of several mitochondrial and blood-derived genes, including Hemoglobin Subunit Beta (*HBB*), Hemoglobin Subunit Alpha (*HBA*), and MT-RNR2 Pseudogene 1 (*MT-RNR2L*) genes, in the EV<sub>PpIX</sub> transcriptome (Figure 5A, Table S4). To develop a stronger comparison, EV<sub>PpIX</sub> was compared to matched total EVs from patient plasma, demonstrating enrichment of GBM oncogenic genes (i.e., GLI family Zinc Finger 3 (*GLI3*) (Matissek & Elsawa, 2020) and RUNX Family Transcription Factor 3 (*RUNX3*) (Zhao et al., 2019)) and downregulation of genes similar to those identified in healthy plasma (Figure 5B). Reactome pathway analysis further describes oncogenic enrichment following EV<sub>PpIX</sub> isolation, demonstrating significant enrichment of Wnt signalling, found to mediate GBM stemness, invasion, and therapeutic resistance (Lee et al., 2016) (Table S4). Further differential expression analysis, comparing EV<sub>PpIX</sub> with matched patient tumour tissue, yields differential expression of only five genes: three enriched in EV<sub>PpIX</sub> and two enriched in tumour (Figure 5C). The similarity in the relative expression across the two sample types suggests representative packaging of the tumour RNA landscape. We have performed linear and planar regression of relative gene expression comparing EV<sub>PpIX</sub> against matched tumour and plasma. Through both analyses, we identify higher similarity between the tumour and EV<sub>PpIX</sub> transcriptome, as opposed to the total plasma vesicular transcriptome (Figure S7A-C). We have additionally assessed the capacity of total plasma EVs for detection of tumour-related genes. Comparing patient plasma against total EVs derived from healthy plasma, we have distinguished enrichment of metabolic regulatory ontologies in healthy plasma contrasted by upregulation of mitochondrial gene expression

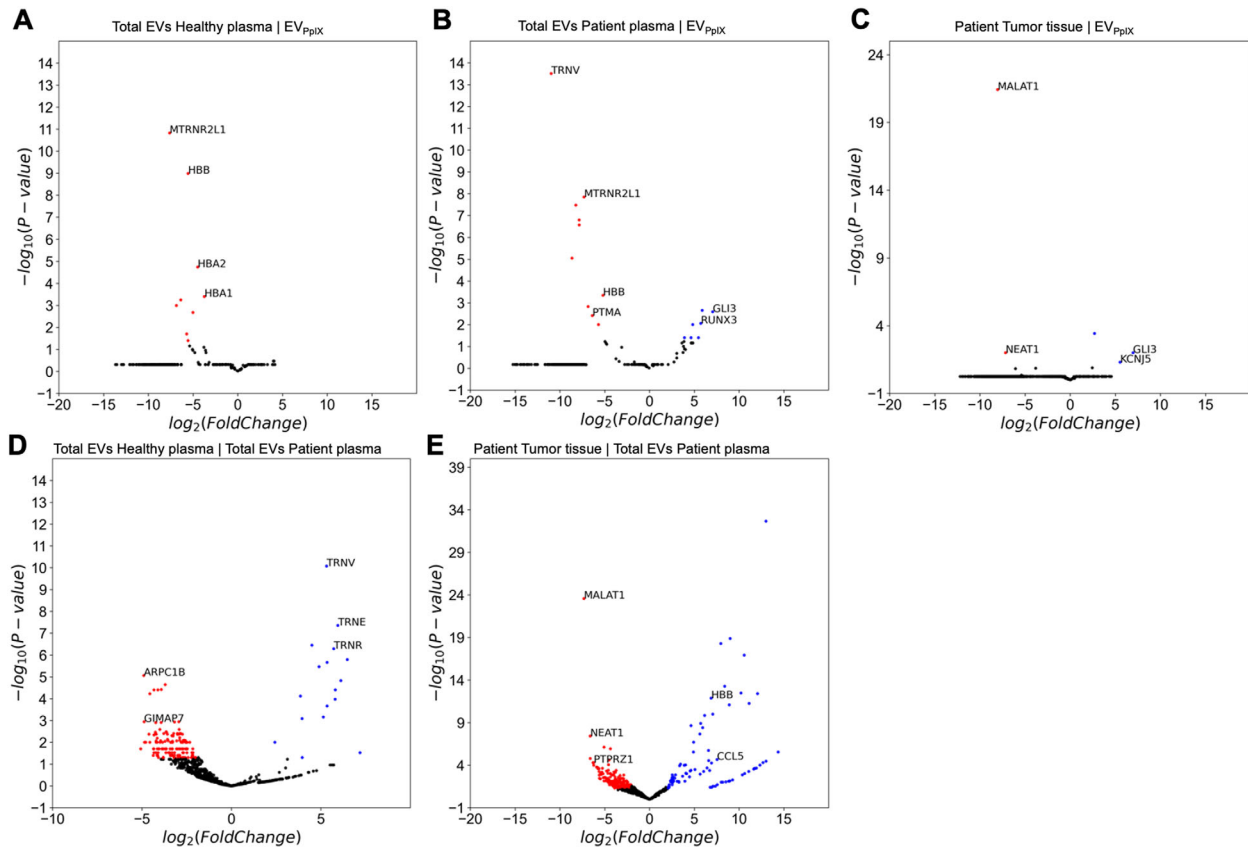


**FIGURE 5** Differential expression of patient and healthy samples. Differential expression analysis of patient  $EV_{PpIX}$  [case] against total EVs from healthy plasma [control] (A), patient  $EV_{PpIX}$  [case] against total EVs from patient plasma [control] (B), patient  $EV_{PpIX}$  [case] against patient tumor tissue [control] (C), total EVs from patient plasma [case] against total EVs from healthy plasma [control], and total EVs from patient plasma [case] against patient tumor tissue [control] was conducted to examine significant gene expression. For each of the differential expression analyses, control groups were established in order of priority (healthy plasma, tumor tissue, and patient plasma) and have been depicted as the left condition above each plot. Significance cutoffs were defined at  $|\log_2(\text{Fold Change})| \geq 2.00$  and  $-\log_{10}(p\text{-value}) \geq 1.30$ , with significantly upregulated genes expressed in blue and significantly downregulated genes expressed in red.

in total EVs from patient plasma (Figure 5D). In fact, all genes demonstrating significant upregulation in the patient plasma EVs are mitochondrial tRNAs. Further examination of expressed RNA biotypes in patient plasma shows 3.6% tRNA composition as compared to 1.1% in healthy plasma, showing increased and upregulated expression of tRNAs in patient plasma EVs. Differential expression analysis of matched plasma EVs compared to the patients' tumour (Figure 5E) showed loss of tumour marker signalling in plasma EVs, such as Glial fibrillary acidic protein (*GFAP*) (Jung et al., 2007), Secreted Phosphoprotein 1 (*SPPI*) (Chen et al., 2019), and Protein Tyrosine Phosphatase Receptor Type Z1 (*PTPRZ1*) (Shi et al., 2017), and increased detection of systemic genes and genes mediating oncogenic paracrine-autocrine signalling (*HBB*, Platelet Factor 4 (*PF4*), and Pro-Platelet Basic Protein (*PPBP*); as well as Chemokine ligand 5 (*CCL5*) (Pan et al., 2017), respectively).

### 3.4 | $EV_{PpIX}$ carry RNA of brain tumour origin

In order to confirm the glioma origin of  $EV_{PpIX}$ , we correlated the gene expression lists for each biotype (patient tumour, patient plasma, patient  $EV_{PpIX}$ , and healthy plasma) with lists of organ-specific elevated genes (Human Protein Atlas (Sjöstedt et al., 2020, The Human Protein Atlas)) to determine the percent alignment with the following organs: brain, breast, lung, stomach, liver, pancreas, intestine, kidney, bladder, and bone. Grouped analysis revealed a significant alignment ( $p < 0.0001$ ) of patient tumour and patient  $EV_{PpIX}$  genetic expression with genes enriched in brain tissue as compared to all other organs (Figure 6A). The plasma transcriptomes for both healthy and patient samples, however, demonstrate comparable levels of alignment between the brain and bone systems. Individual statistical analysis within biotypes and across organs also identified brain specificity within the  $PpIX$  transcriptome (Figure S8). Further analysis of putative GBM relevant genes revealed a list of 10 mRNAs that are common to  $EV_{PpIX}$  and tumour tissue, but are not found in the matched plasma (Table 3) (Ferguson et al., 2016, Jiao et al., 2020, Louis et al., 2021, McAvoy et al., 2021, Sakthikumar et al., 2020).

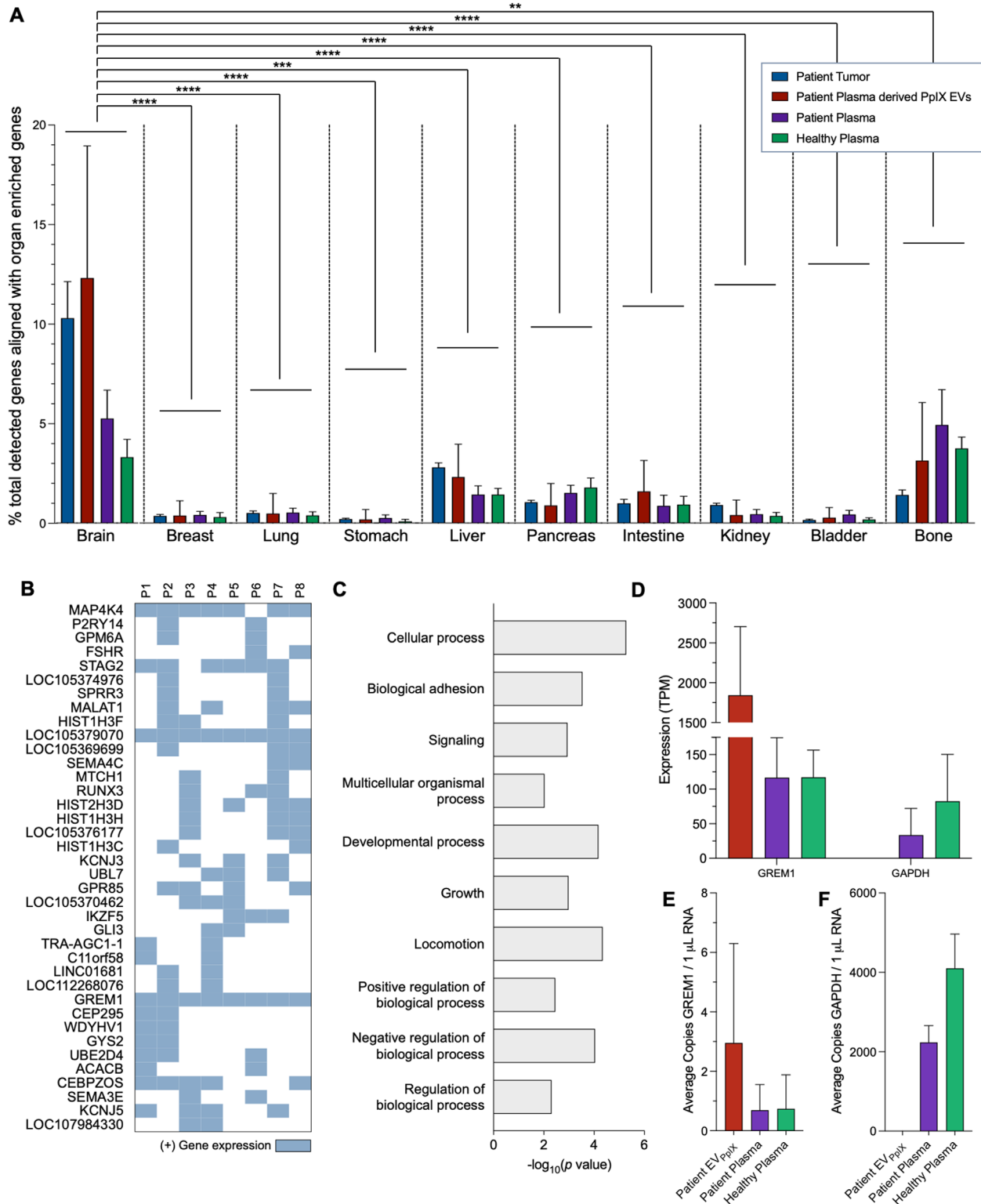


**FIGURE 6** EV<sub>ppIX</sub> origin identification and PCR validation of notable EV genes. Gene lists with organ-specific, elevated expression were obtained via the Human Protein Atlas (Sjöstedt et al., 2020, The Human Protein Atlas) and compared against the cumulative gene lists for each biological type: patient tumor, patient EV<sub>ppIX</sub>, patient plasma, and healthy plasma (A). Percentage alignment was calculated from the [number of genes aligned to the elevated expression list] out of the [total number genes detected] in each biotype. Significance was determined at a cutoff of  $p \leq 0.05$ . Expression of genes common across all patient EV<sub>ppIX</sub> was determined (B) and the resulting list was analyzed using gene ontology (C). The gene common to both patient EV<sub>ppIX</sub> and the notable genes in cell line subpopulations was considered for assay validation. *GREM1* expression levels (TPM) were compiled for comparative use (D). *GAPDH* expression was extracted for use as a control. The validation study was performed on 100,000 sorted patient EV<sub>ppIX</sub> and a cohort of patient and healthy total plasma EVs ( $n = 3$ , respectively). ddPCR for the *GREM1* assay (E) was performed multiplexed with *GAPDH* (F) and expression levels were compared across biotypes.

**TABLE 3** GBM relevant genes common to the transcriptome of EV<sub>PpIX</sub> and tumour

(average expression in TPM)	Tumour	PpIX EV	Patient plasma	Healthy plasma
GLI3	20.41	5736.56	0	0
MAP2	138.56	478.01	0	4.8
PCLO	33.90	267.67	0	0
SEMA4C	5.01	336.90	0	0
ZNF121	21.90	478.01	0	0
ZNF37A	35.45	267.67	0	0
ZNF462	87.60	507.87	0	0
ZNF649	4.17	351.86	0	0
ZNF764	10.02	299.94	0	0
ZNF777	8.20	135.37	0	0

Subsequently, we sought distinct, recurring genes from the EV<sub>PpIX</sub> transcriptome across the patient cohort and have compiled a series of genes that are expressed in two patients or more (Figure 6B). Ontological analysis of these genes implicates cellular process regulation as the most significantly influenced gene ontology, suggesting dysregulation of cellular proliferation, a cancer hallmark (Figure 6C). Specifically, *GREM1* was found to be enriched in patient EV<sub>PpIX</sub> and demonstrated consistent expression in the EV<sub>PpIX</sub> derived from all cell lines as well. As such, we selected *GREM1* for PCR validation. The housekeeping gene Glyceraldehyde 3-phosphate dehydrogenase (*GAPDH*) was measured in parallel, for comparison. From the sequencing, expression levels of the genes in EV<sub>PpIX</sub>, patient, and healthy plasma were extracted for parallel comparison (Figure 6D). Droplet digital PCR (ddPCR) was performed using a multiplexed *GREM1*-FAM and *GAPDH*-VIC assay, with normalization performed with respect to 1  $\mu$ L of RNA. We show that sorting and quantification of EV<sub>PpIX</sub> results in increased *GREM1* detection, as compared to total EVs from both healthy and patient plasma (Figure 6E). Furthermore, *GAPDH* detection in the EV<sub>PpIX</sub> is negligible as compared to detection in patient and healthy plasma (0.4 copies/1  $\mu$ l RNA, 2270.54 copies/1  $\mu$ l RNA, and 4399 copies/1  $\mu$ l RNA, respectively; Figure 6F). These provide a reflection of the expression levels as defined by the sequencing results, supporting the notion of enrichment of GBM-related genes through EV<sub>PpIX</sub> isolation.

## 4 | DISCUSSION

EV heterogeneity remains an obstacle in the analysis of tumour-related genes, especially in the context of biofluids (Willms et al., 2018). Furthermore, the broad spectrum of EV subpopulations and their cargo has been shown to depend on the cell of origin, environmental conditions, and pathways of biogenesis (Abels & Breakefield, 2016). Previous literature on EV subpopulations in melanoma has established subpopulation-specific proteomes and RNA cargo (Willms et al., 2016). We have previously shown a positive correlation between tumour presence and EV<sub>PpIX</sub> following 5-ALA ingestion in patients with GBM and in GBM animal models (Jones et al., 2019). We have now extended our analysis to assess five subpopulations of EVs derived from glioblastoma cell lines: EV<sub>CFDA</sub>, EV<sub>CD63</sub>, EV<sub>CD9</sub>, EV<sub>EGFR</sub>, and EV<sub>PpIX</sub>. Comparisons of their prevalence revealed cell line-unique production, with EV<sub>CD9</sub> being the highest, followed by EV<sub>CD63</sub>, EV<sub>EGFR</sub>, and EV<sub>PpIX</sub>. Previous studies investigating EV<sub>CD9</sub> and EV<sub>CD63</sub> have identified similar results, demonstrating higher EV<sub>CD9</sub> production over EV<sub>CD63</sub> (Ricklefs et al., 2019). Comparison of two EGFR<sup>WT</sup> cell lines (Gli36<sup>EGFRwt</sup> and U87) show a distinct drop in EV<sub>EGFR</sub> production following [EV<sub>CD9</sub>] increase, which aligns with previous reports of CD9-induced negative regulation of EGFR (Murayama et al., 2008). Interestingly, in the presence of the EGFRvIII mutation, however, the EV<sub>EGFR</sub> population is not significantly affected by the dramatic increase in EV<sub>CD9</sub> (EV<sub>EGFR</sub>/EV<sub>CD9</sub>: (Gli36<sup>EGFRwt</sup>) 3.1E5/2.9E6 EVs/ml; (Gli36<sup>EGFRvIII</sup>) 3.4E5/4.1E6 EVs/ml). This not only confirms previous findings of the effect of cellular EGFRvIII on EV<sub>CD9</sub> expression (Choi et al., 2018) but also reveals an alternate interaction between CD9 and EGFRvIII that prevents EGFR downregulation. Further assessment of these interactions will be required to delineate the biogenetic mechanism.

We also show that 5-ALA dosing does not significantly alter EV phenotype, that is, total EV production or size distribution, with only one cell line, Gli36<sup>EGFRwt</sup>, showing a significant increase in EV<sub>CD63</sub>. Furthermore, transcriptome analysis of EV RNA, following 5-ALA dosing, closely resembled that of EV RNA from mock-dosed cells. All of this supports the concept that 5-ALA does not significantly influence the phenotype and genotype of cells or EVs and may be reliably used to study and monitor GBM progression.

We found that each subpopulation bears unique RNA species distributions, suggesting that the varying EV ontogenies may influence EV subpopulation-specific cargo encapsulation. Previously reported EV RNA landscapes have found an approximate

4:1 ratio of non-coding RNAs to mRNAs (Wei et al., 2017) and have also established a highly diverse small RNA population that encompasses microRNAs (miRNAs), tRNAs, Y RNAs, snRNAs, snoRNAs, and scRNAs (Wei et al., 2017). Across all the analysed subpopulations, we observe a relative abundance of lncRNAs and mRNAs at an opposite ratio (2:8), which is likely attributed to the poly-adenylated RNA-enrichment library preparation process utilized. We also see several similar small RNA classes as previously identified, including all of those mentioned above. The relative abundance of each class, however, varied significantly. Deviations identified in our study may be attributed to variations in cell culture, methods of EV collection, and RNA extractions protocols, but most importantly, the library preparation protocol and ensuing sequencing. Through this study, we provide a primary focus on long RNAs. Further analysis of the small RNA populations across EV subpopulations will require small RNA library preparation and sequencing.

Interestingly, EV<sub>PpIX</sub> derived from GBM cell lines and those sorted from GBM patient plasma reveal similar long RNA profiles, possibly suggesting similar ontogenies. Specifically, they contain higher levels of lncRNAs, long implicated in GBM development via sustained proliferation (Liao et al., 2019), immune evasion (Wu et al., 2020), and bear therapeutic potential (Stackhouse et al., 2020). We also found that the five different subpopulations enrich for unique cargo and have a very low number of overlapping genes. Specific assessment of enriched regions demonstrating phylogenetic similarity within each subpopulation (in vitro) suggests pathway-specific packaging into EVs and implicates the power of isolating subpopulations for functional analysis. Specifically, ontologies enriched in total conditioned media were found to involve cell cycle, growth, and biosynthetic processes, whereas enriched regions within each subpopulation provided enrichment of unique pathways with prognostic capacity. Moreover, 78% of the significant pathways associated with the cell line-derived EV<sub>PpIX</sub> transcriptome relates to oncogenic pathways such as EGFR inhibitor resistance (Guo et al., 2017), MAPK signalling (Zohrabian et al., 2009), apoptosis regulation (Valdés-Rives et al., 2017), mammalian target of rapamycin (mTOR) signalling (Akhavan et al., 2010), and the Phosphoinositide 3-kinase/Akt strain transforming (PI3K-Akt) signalling pathway (Li et al., 2016). The enrichment of these pathways in only 100,000 EV<sub>PpIX</sub> aptly demonstrates their tumour-derived nature.

The glioblastoma patient plasma derived EV<sub>PpIX</sub> transcriptome was then directly overlaid with genes enriched in several organs, including brain, breast, lung, and liver. We determined a significant degree of alignment with brain specific genes while other organs were not significantly represented. Furthermore, genes upregulated in the primary tumour, such as SOX2 Overlapping Transcript (*SOX2-OT*) (Su et al., 2017), Metastasis Associated Lung Adenocarcinoma Transcript 1 (*MALAT1*) (Chen et al., 2017), Autophagy-Related Protein 1 Homolog (*ATG1*) (Zhou et al., 2020, Zhou et al., 2021), were also enriched in EV<sub>PpIX</sub> (average TPM: 33.46, 237.85, 23.89, respectively) as compared to patient plasma-derived EVs (average TPM: 0.15, 11.36, 5.68, respectively). Several genes which influence GBM progression and therapeutic resistance were also identified in more than 50% of the EV<sub>PpIX</sub> from patients, including *GREM1* (Guan et al., 2017), mitogen-activated protein 4 kinase 4 (*MAP4K4*) (Prolo et al., 2019), Semaphorin 4C (*SEMA4C*) (Angelucci et al., 2019), and Stromal Antigen 2 (*STAG2*) (Bailey et al., 2014). Putative GBM-specific genes (Ferguson et al., 2016, Jiao et al., 2020, Louis et al., 2021, McAvoy et al., 2021, Sakthikumar et al., 2020) included *GLI3*, *SEMA4C*, and several from the zinc-finger protein family (ZNF). Zinc finger proteins have been extensively defined in systemic cancer progression, including in gliomas and glioblastomas (Jen & Wang, 2016). Notably, TCGA analysis of *ZNF764*, found only in EV<sub>PpIX</sub> and tumour tissue, demonstrates significant prognostic value at three (25%, 50%, and 75%) expression thresholds (Figure S9). This is highly significant as we further confirm the validity of EV<sub>PpIX</sub> isolation to examine GBM-specific gene signatures. This avenue of enrichment shows increased prognostic and diagnostic capacity, especially as isolation of only 250,000 EVs yield significant genotypic findings. Further optimization of sorting capacity will greatly empower the utility of tumour-specific EVs for non-invasive biopsy.

KEGG pathway analysis of common EV<sub>PpIX</sub> genes revealed several significant cancer-promoting pathways including WNT (Lee et al., 2016), Runt-Related Transcription Factor 1 (*RUNX1*) (Sangpairoj et al., 2017), Notch signalling (Bazzoni & Bentivegna, 2019), and amino acid metabolism. Amino acids play a role in tumour epigenetic regulation, prognostic identification, and therapeutic targeting (Lieu et al., 2020). In particular, the Aspartoacylase gene (*ASPA*) acts within the alanine and asparagine-glutamine networks and influences GBM patient survival (Panosyan et al., 2017). Other genes found within EV<sub>PpIX</sub> that contribute to amino acid metabolism include Methylthioadenosine Phosphorylase (*MTAP*) and Dehydrogenase E1 And Transketolase Domain Containing 1 (*DHTKDI*), which moderate cancer stemness (Hansen et al., 2019) and cell proliferation and apoptosis (Xu et al., 2013), respectively.

We have identified one mRNA, *GREM1*, expressed in EV<sub>PpIX</sub> derived from cell lines and patient tumour. *GREM1* is known to promote tumour cell proliferation and negatively modulate pro-differentiation processes (Yan et al., 2014). Identification of this gene in EV<sub>PpIX</sub>, in vitro and in vivo, potentiates its use as a common marker of tumour characterization. Using a droplet digital PCR (ddPCR) assay, we detected similar levels of *GREM1* in total EVs (~10<sup>11</sup> EVs; 1 ml) derived from patient and healthy plasma. However, sorting and subsequent downstream analysis of only 10<sup>5</sup> EV<sub>PpIX</sub> showed enhanced detection of *GREM1*. Along with the ddPCR-detected *GAPDH* (housekeeping gene) expression levels, we were able to validate the pattern of expression as found via sequencing. With this, we show cancer genetic enrichment in EV<sub>PpIX</sub> as compared to total patient plasma and total healthy plasma EVs, implicating the ability for enhanced tumour-specific gene detection via EV<sub>PpIX</sub> isolation.

## 5 | CONCLUSION

The EV landscape is widely accepted as diverse in biological fluids due to the nature of EV biogenesis. In the context of liquid biopsy and identification of rare mutations, it becomes imperative to implement modalities of tumour specific EV enrichment. Our study shows that we can (i) identify, sort, and distinctively analyse sorted EVs, (ii) discriminate EV subpopulations with unique expression regions as compared to the total plasma-derived vesicular transcriptome, and (iii) facilitate quantification of targeted, cancer-specific cargo. Importantly, 5-ALA metabolism-induced PpIX endogenous fluorescence in EVs specifically provides an avenue for tumour-specific transcriptome analysis in biofluids and paves the way for the development of other endogenously fluorescent cancer markers. The isolation of fluorescent PpIX EVs enriches the cancer-related transcriptome, empowering non-invasive longitudinal diagnosis and monitoring that bears potential to supplement imaging-based detection of disease progression.

### AUTHOR CONTRIBUTIONS

Tiffany Hsia: Data curation; Formal analysis; Investigation; Methodology; Software; Validation; Visualization; Writing – original draft; Writing – review & editing. Anudeep Yekula: Data curation; Formal analysis; Investigation; Methodology; Software; Validation; Visualization; Writing – original draft; Writing – review & editing. S. Maheen Batool: Data curation; Investigation; Methodology; Writing – review & editing. Yulia B. Rosenfeld: Investigation; Writing – review & editing. Dong Gil You: Investigation; Methodology; Writing – review & editing. Ralph Weissleder: Investigation; Writing – review & editing. Hakho Lee: Investigation; Writing – review & editing. Bob S. Carter: Conceptualization; Data curation; Formal analysis; Funding acquisition; Investigation; Methodology; Project administration; Resources; Software; Supervision; Validation; Visualization; Writing – original draft; Writing – review & editing. Leonora Balaj: Conceptualization; Data curation; Formal analysis; Funding acquisition; Investigation; Methodology; Project administration; Resources; Software; Supervision; Validation; Visualization; Writing – original draft; Writing – review & editing.

### ACKNOWLEDGEMENTS

We would like to thank the patients and their families for their participation in this study. This work is supported by grants P01 CA069246 (B.S.C., R.W.), R01 CA239078 (B.S.C., H.L.), R01 CA237500 (B.S.C., L.B., H.L.), U01 CA230697 (B.S.C., L.B.) and Rappaport Foundation (L.B.). The funding sources had no role in either the writing of the manuscript or the decision to submit the manuscript for publication. The author has not been paid to write this article. The corresponding author has full access to the manuscript and assumes final responsibility for the decision to submit for publication.

### DATA AVAILABILITY STATEMENT

Data and code used in manuscript preparation is available upon reasonable request.

### ORCID

Tiffany Hsia  <https://orcid.org/0000-0003-4526-2605>

Anudeep Yekula  <https://orcid.org/0000-0002-0713-0292>

S. Maheen Batool  <https://orcid.org/0000-0002-3264-1182>

Dong Gil You  <https://orcid.org/0000-0002-9508-6454>

Leonora Balaj  <https://orcid.org/0000-0003-0931-9715>

### REFERENCES

- Abels, E. R., & Breakefield, X. O. (2016). Introduction to extracellular vesicles: Biogenesis, RNA cargo selection, content, release, and uptake. *Cell. Mol. Neurobiol.*, 36, 301–312.
- Akhavan, D., Cloughesy, T. F., & Mischel, P. S. (2010). mTOR signaling in glioblastoma: lessons learned from bench to bedside. *Neuro-oncol.*, 12, 882–889.
- Angelucci, C., Lama, G., & Sica, G. (2019). Multifaceted functional role of semaphorins in glioblastoma. *International Journal of Molecular Sciences*, 20, 2144.
- Bailey, M. L., O'neil, N. J., Van Pel, D. M., Solomon, D. A., Waldman, T., & Hieter, P. (2014). Glioblastoma cells containing mutations in the cohesin component STAG2 are sensitive to PARP inhibition. *Molecular Cancer Therapeutics*, 13, 724–732.
- Bazzoni, R., & Bentivegna, A. (2019). Role of Notch signaling pathway in glioblastoma pathogenesis. *Cancers*, 11, 292.
- Beer, K. B., & Wehman, A. M. (2017). Mechanisms and functions of extracellular vesicle release in vivo—What we can learn from flies and worms. *Cell Adhesion & Migration*, 11, 135–150.
- Chelakkot, V. S., Liu, K., Yoshioka, E., Saha, S., Xu, D., Licursi, M., Dorward, A., & Hirasawa, K. (2020). MEK reduces cancer-specific PpIX accumulation through the RSK-ABCBI and HIF-1 $\alpha$ -FECH axes. *Science Reports*, 10, 22124.
- Chen, W. W., Balaj, L., Liao, L. M., Samuels, M. L., Kotsopoulos, S. K., Maguire, C. A., Loguidice, L., Soto, H., Garrett, M., Zhu, L. D., Sivaraman, S., Chen, C., Wong, E. T., Carter, B. S., Hochberg, F. H., Breakefield, X. O., & Skog, J. (2013). BEAMing and droplet digital PCR analysis of mutant IDH1 mRNA in glioma patient serum and cerebrospinal fluid extracellular vesicles. *Mol. Ther. Nucleic Acids*, 2, e109.
- Chen, W., Xu, X.-K., Li, J.-L., Kong, K.-K., Li, H., Chen, C., He, J., Wang, F., Li, P., Ge, X.-S., & Li, F.-C. (2017). MALAT1 is a prognostic factor in glioblastoma multiforme and induces chemoresistance to temozolomide through suppressing miR-203 and promoting thymidylate synthase expression. *Oncotarget*, 8, 22783–22799.

- Chen, P., Zhao, D., Li, J., Liang, X., Li, J., Chang, A., Henry, V. K., Lan, Z., Spring, D. J., Rao, G., Wang, Y. A., & Depinho, R. A. (2019). Symbiotic macrophage-glioma cell interactions reveal synthetic lethality in PTEN-Null glioma. *Cancer Cell*, 35, 868–884.e6.e6.
- Choi, D., Montermini, L., Kim, D.-K., Meehan, B., Roth, F. P., & Rak, J. (2018). The impact of oncogenic EGFRvIII on the proteome of extracellular vesicles released from glioblastoma cells. *Molecular & Cellular Proteomics*, 17, 1948–1964.
- Das, S., & Marsden, P. A. (2013). Angiogenesis in glioblastoma. *New England Journal of Medicine*, 369, 1561–1563.
- De Oliveira, G. P., Zigon, E., Rogers, G., Davodian, D., Lu, S., Jovanovic-Talman, T., Jones, J., Tigges, J., Tyagi, S., & Ghiran, I. C. (2020). Detection of extracellular vesicle RNA using molecular beacons. *iScience*, 23, 100782.
- Domínguez-Vigil, I. G., Moreno-Martánez, A. K., Wang, J. Y., Roehrl, M. H. A., & Barrera-Saldaña, H. A. (2018). The dawn of the liquid biopsy in the fight against cancer. *Oncotarget*, 9, 2912–2922.
- Ferguson, S. D., Xiu, J., Weathers, S.-P., Zhou, S., Kesari, S., Weiss, S. E., Verhaak, R. G., Höhl, R. J., Barger, G. R., Reddy, S. K., & Heimberger, A. B. (2016). GBM-associated mutations and altered protein expression are more common in young patients. *Oncotarget*, 7, 69466–69478.
- Figueroa, J. M., & Carter, B. S. (2018). Detection of glioblastoma in biofluids. *Journal of Neurosurgery*, 129, 334–340.
- Ghaemmaghami, A. B., Mahjoubin-Tehran, M., Movahedpour, A., Morshedi, K., Sheida, A., Taghavi, S. P., Mirzaei, H., & Hamblin, M. R. (2020). Role of exosomes in malignant glioma: microRNAs and proteins in pathogenesis and diagnosis. *Cell Commun. Signal*, 18, 120.
- Guan, Y., Cheng, W., Zou, C., Wang, T., & Cao, Z. (2017). Gremlin1 promotes carcinogenesis of glioma in vitro. *Clinical and Experimental Pharmacology & Physiology*, 44, 244–256.
- Guo, G., Gong, K., Ali, S., Ali, N., Shallwani, S., Hatanpaa, K. J., Pan, E., Mickey, B., Burma, S., Wang, D. H., Kesari, S., Sarkaria, J. N., Zhao, D., & Habib, A. A. (2017). A TNF-JNK-Axl-ERK signaling axis mediates primary resistance to EGFR inhibition in glioblastoma. *Nature Neuroscience*, 20, 1074–1084.
- Hadjipanayis, C. G., & Stummer, W. (2019). 5-ALA and FDA approval for glioma surgery. *Journal of Neuro-Oncology*, 141, 479–486.
- Hansen, L. J., Sun, R., Yang, R., Singh, S. X., Chen, L. H., Pirozzi, C. J., Moure, C. J., Hemphill, C., Carpenter, A. B., Healy, P., Ruger, R. C., Chen, C.-P. J., Greer, P. K., Zhao, F., Spasojevic, I., Grenier, C., Huang, Z., Murphy, S. K., Mclendon, R. E., ... He, Y. (2019). MTAP loss promotes stemness in glioblastoma and confers unique susceptibility to purine starvation. *Cancer Research*, 79, 3383–3394.
- Inda, M.-D.-M., Bonavia, R., & Seoane, J. (2014). Glioblastoma multiforme: a look inside its heterogeneous nature. *Cancers*, 6, 226–239.
- Ishizuka, M., Abe, F., Sano, Y., Takahashi, K., Inoue, K., Nakajima, M., Kohda, T., Komatsu, N., Ogura, S.-I., & Tanaka, T. (2011). Novel development of 5-aminolevulinic acid (ALA) in cancer diagnoses and therapy. *International Immunopharmacology*, 11, 358–365.
- Jen, J., & Wang, Y.-C. (2016). Zinc finger proteins in cancer progression. *Journal of Biomedical Science*, 23, 53.
- Jiao, F., Li, Z., He, C., Xu, W., Yang, G., Liu, T., Shen, H., Cai, J., Anastas, J. N., Mao, Y., Yu, Y., Lan, F., Shi, Y. G., Jones, C., Xu, Y., Baker, S. J., Shi, Y., & Guo, R. (2020). RACK7 recognizes H3.3G34R mutation to suppress expression of MHC class II complex components and their delivery pathway in pediatric glioblastoma. *Science Advances*, 6, eaba2113.
- Jones, P. S., Yekula, A., Lansbury, E., Small, J. L., Ayinon, C., Mordecai, S., Hochberg, F. H., Tigges, J., Delcuze, B., Charest, A., Ghiran, I., Balaj, L., & Carter, B. S. (2019). Characterization of plasma-derived protoporphyrin-IX-positive extracellular vesicles following 5-ALA use in patients with malignant glioma. *EBioMedicine*, 48, 23.
- Jung, C. S., Foerch, C., Schanzer, A., Heck, A., Plate, K. H., Seifert, V., Steinmetz, H., Raabe, A., & Sitzer, M. (2007). Serum GFAP is a diagnostic marker for glioblastoma multiforme. *Brain*, 130, 3336–3341.
- Lane, R., Simon, T., Vintu, M., Solkin, B., Koch, B., Stewart, N., Benstead-Hume, G., Pearl, F. M. G., Critchley, G., Stebbing, J., & Giamas, G. (2019). Cell-derived extracellular vesicles can be used as a biomarker reservoir for glioblastoma tumor subtyping. *Commun Biol*, 2, 315.
- Lee, Y., Lee, J.-Ku., Ahn, S. H., Lee, J., & Nam, D.-H. (2016). WNT signaling in glioblastoma and therapeutic opportunities. *Laboratory Investigation*, 96, 137–150.
- Li, X., Wu, C., Chen, N., Gu, H., Yen, A., Cao, L., Wang, E., & Wang, L. (2016). PI3K/Akt/mTOR signaling pathway and targeted therapy for glioblastoma. *Oncotarget*, 7, 33440–33450.
- Liao, Y., Zhang, B., Zhang, T., Zhang, Y., & Wang, F. (2019). LncRNA GATA6-AS promotes cancer cell proliferation and inhibits apoptosis in glioma by downregulating lncRNA TUG1. *Cancer Biotherapy & Radiopharmaceuticals*, 34, 660–665.
- Lieu, E. L., Nguyen, T., Rhyne, S., & Kim, J. (2020). Amino acids in cancer. *Experimental & Molecular Medicine*, 52, 15–30.
- Louis, D. N., Perry, A., Wesseling, P., Brat, D. J., Cree, I. A., Figarella-Branger, D., Hawkins, C., Ng, H. K., Pfister, S. M., Reifenberger, G., Soffietti, R., Von Deimling, A., & Ellison, D. W. (2021). The 2021 WHO classification of tumors of the central nervous system: A summary. *Neuro-oncol*, 23, 1231–1251.
- Maas, S. L. N., Van Solinge, T. S., Schnoor, R., Yekula, A., Senders, J. T., De Vrij, J., Robe, P., Carter, B. S., Balaj, L., Arkesteijn, G. J. A., Nolte-t Hoen, E. N. M., Broekman, & M. L. D. (2020). Orally administered 5-aminolevulinic acid for isolation and characterization of circulating tumor-derived extracellular vesicles in glioblastoma patients. *Cancers*, 12, 3297.
- Matissek, S. J., & Elswa, S. F. (2020). GLI3: a mediator of genetic diseases, development and cancer. *Cell Commun. Signal*, 18, 54.
- McAvoy, M., Prieto, P. C., Kaczmarzyk, J. R., Fernández, I. S., McNulty, J., Smith, T., Yu, K.-H., Gormley, W. B., & Arnaout, O. (2021). Classification of glioblastoma versus primary central nervous system lymphoma using convolutional neural networks. *Science Reports*, 11, 15219.
- Murayama, Y., Shinomura, Y., Oritani, K., Miyagawa, J.-I., Yoshida, H., Nishida, M., Katsube, F., Shiraga, M., Miyazaki, T., Nakamoto, T., Tsutsui, S., Tamura, S., Higashiyama, S., Shimomura, I., & Hayashi, N. (2008). The tetraspanin CD9 modulates epidermal growth factor receptor signaling in cancer cells. *Journal of Cellular Physiology*, 216, 135–143.
- O'Neill, C. P., Gilligan, K. E., & Dwyer, R. M. (2019). Role of extracellular vesicles (EVs) in cell stress response and resistance to cancer therapy. *Cancers*, 11, 136.
- Ostrom, Q. T., Patil, N., Cioffi, G., Waite, K., Kruchko, C., & Barnholtz-Sloan, J. S. (2020). CBTRUS statistical report: Primary brain and other central nervous system tumors diagnosed in the United States in 2013–2017. *Neuro-oncol*, 22, iv1–iv96.
- Pan, Y., Smithson, L. J., Ma, Y., Hambarzumyan, D., & Gutmann, D. H. (2017). Ccl5 establishes an autocrine high-grade glioma growth regulatory circuit critical for mesenchymal glioblastoma survival. *Oncotarget*, 8, 32977–32989.
- Panosyan, E. H., Lin, H. J., Koster, J., & Lasky, J. L. 3rd. (2017). In search of druggable targets for GBM amino acid metabolism. *BMC cancer*, 17, 162.
- Prolo, L. M., Li, A., Owen, S. F., Parker, J. J., Foshay, K., Nitta, R. T., Morgens, D. W., Bolin, S., Wilson, C. M., Vega, L. J. C. M., Luo, E. J., Nwagbo, G., Waziri, A., Li, G., Reimer, R. J., Bassik, M. C., & Grant, G. A. (2019). Targeted genomic CRISPR-Cas9 screen identifies MAP4K4 as essential for glioblastoma invasion. *Science Reports*, 9, 14020.
- Ricklefs, F. L., Maire, C. L., Reimer, R., Dührsen, L., Kolbe, K., Holz, M., Schneider, E., Rissiek, A., Babayan, A., Hille, C., Pantel, K., Krasemann, S., Glatzel, M., Heiland, D. H., Flitsch, J., Martens, T., Schmidt, N. O., Peine, S., Breakefield, X. O., ... Lamszus, K. (2019). Imaging flow cytometry facilitates multiparametric characterization of extracellular vesicles in malignant brain tumours. *J Extracell Vesicles*, 8, 1588555.
- Robinson, M. D., & Oshlack, A. (2010). A scaling normalization method for differential expression analysis of RNA-seq data. *Genome Biology*, 11, R25.
- Roy, S., Lin, H.-Y., Chou, C.-Y., Huang, C.-H., Small, J., Sadik, N., Ayinon, C., Lansbury, E., Cruz, L., Yekula, A., Jones, P., Balaj, L., & Carter, B. (2019). Navigating the landscape of tumor extracellular vesicle heterogeneity. *International Journal of Molecular Sciences*, 20, 1349.

- Sakthikumar, S., Roy, A., Haseeb, L., Pettersson, M. E., Sundström, E., Marinescu, V. D., Lindblad-Toh, K., & Forsberg-Nilsson, K. (2020). Whole-genome sequencing of glioblastoma reveals enrichment of non-coding constraint mutations in known and novel genes. *Genome biology*, *21*, 127.
- Sangpairoj, K., Vivithanaporn, P., Apisawetakan, S., Chongthammakun, S., Sobhon, P., & Chaithirayanon, K. (2017). RUNX1 regulates migration, invasion, and angiogenesis via p38 MAPK pathway in human glioblastoma. *Cellular and Molecular Neurobiology*, *37*, 1243–1255.
- Shankar, G. M., Balaj, L., Stott, S. L., Nahed, B., & Carter, B. S. (2017). Liquid biopsy for brain tumors. *Expert Review of Molecular Diagnostics*, *17*, 943–947.
- Shi, Y., Ping, Y.-F., Zhou, W., He, Z.-C., Chen, C., Bian, B.-S.-J., Zhang, L., Chen, L., Lan, X., Zhang, X.-C., Zhou, K., Liu, Q., Long, H., Fu, T.-W., Zhang, X.-N., Cao, M.-Fu., Huang, Z., Fang, X., Wang, X., ... Bian, X.-W. (2017). Tumour-associated macrophages secrete pleiotrophin to promote PTPRZ1 signalling in glioblastoma stem cells for tumour growth. *Nature Communication*, *8*, 15080.
- Sjöstedt, E., Zhong, W., Fagerberg, L., Karlsson, M., Mitsios, N., Adori, C., Oksvold, P., Edfors, F., Limiszewska, A., Hikmet, F., Huang, J., Du, Y., Lin, L., Dong, Z., Yang, L., Liu, X., Jiang, H., Xu, X., Wang, J., ... Mulder, J. (2020). An atlas of the protein-coding genes in the human, pig, and mouse brain. *Science*, *367*, .
- Skog, J., Würdinger, T., Van Rijn, S., Meijer, D. H., Gainche, L., Curry, W. T., Carter, B. S., Krichevsky, A. M., & Breakefield, X. O. (2008). Glioblastoma microvesicles transport RNA and proteins that promote tumour growth and provide diagnostic biomarkers. *Nature Cell Biology*, *10*, 1470–1476.
- Sottoriva, A., Spiteri, I., Piccirillo, S. G. M., Touloumis, A., Collins, V. P., Marioni, J. C., Curtis, C., Watts, C., & Tavaré, S. (2013). Intratumor heterogeneity in human glioblastoma reflects cancer evolutionary dynamics. *PNAS*, *110*, 4009–4014.
- Stackhouse, C. T., Gillespie, G. Y., & Willey, C. D. (2020). Exploring the roles of lncRNAs in GBM pathophysiology and their therapeutic potential. *Cells*, *9*, 2369.
- Su, R., Cao, S., Ma, J., Liu, Y., Liu, X., Zheng, J., Chen, J., Liu, L., Cai, H., Li, Z., Zhao, L., He, Q., & Xue, Y. (2017). Knockdown of SOX2OT inhibits the malignant biological behaviors of glioblastoma stem cells via up-regulating the expression of miR-194-5p and miR-122. *Molecular cancer*, *16*, 171.
- Théry, C., Witwer, K. W., Aikawa, E., Alcaraz, M. J., Anderson, J. D., Andriantsitohaina, R., Antoniou, A., Arab, T., Archer, F., Atkin-Smith, G. K., Ayre, D. C., Bach, J.-M., Bachurski, D., Baharvand, H., Balaj, L., Baldacchino, S., Bauer, N. N., Baxter, A. A., Bebawy, M., ... Zuba-Surma, E. K. (2018). Minimal information for studies of extracellular vesicles 2018 (MISEV2018): A position statement of the International Society for Extracellular Vesicles and update of the MISEV2014 guidelines. *J Extracell Vesicles*, *7*, 1535750.
- Tricarico, C., Clancy, J., & D'souza-Schorey, C. (2017). Biology and biogenesis of shed microvesicles. *Small GTPases*, *8*, 220–232.
- Valdés-Rives, S. A., Casique-Aguirre, D., Germán-Castelán, L., & Velasco-Velázquez, M. A., & González-Arenas, A. (2017). Apoptotic signaling pathways in glioblastoma and therapeutic implications. *Biomed Res. Int.*, *2017*, 1.
- Wei, Z., Batagov, A. O., Schinelli, S., Wang, J., Wang, Y., El Fatimy, R., Rabinovsky, R., Balaj, L., Chen, C. C., Hochberg, F., Carter, B., Breakefield, X. O., & Krichevsky, A. M. (2017). Coding and noncoding landscape of extracellular RNA released by human glioma stem cells. *Nature Communication*, *8*, 1–15.
- Weller, M., Van Den Bent, M., Preusser, M., Le Rhun, E., Tonn, J. C., Minniti, G., Bendszus, M., Balana, C., Chinot, O., Dirven, L., French, P., Hegi, M. E., Jakola, A. S., Platten, M., Roth, P., Rudà, R., Short, S., Smits, M., Taphoorn, M. J. B., ... Wick, W. (2021). EANO guidelines on the diagnosis and treatment of diffuse gliomas of adulthood. *Nature reviews Clinical oncology*, *18*, 170–186.
- Welsh, J. A., Horak, P., Wilkinson, J. S., Ford, V. J., Jones, J. C., Smith, D., Holloway, J. A., & Englyst, N. A. (2020). FCMPASS software aids extracellular vesicle light scatter standardization. *Cytometry Part A: the journal of the International Society for Analytical Cytology*, *97*, 569–581.
- Willms, E., Johansson, H. J., Mäger, I., Lee, Y., Blomberg, K. E. M., Sadik, M., Alaarg, A., Smith, C. I. E., Lehtiö, J., El Andaloussi, S., Wood, M. J. A., & Vader, P. (2016). Cells release subpopulations of exosomes with distinct molecular and biological properties. *Science Reports*, *6*, 22519.
- Willms, E., Cabañas, C., Mäger, I., Wood, M. J. A., & Vader, P. (2018). Extracellular vesicle heterogeneity: Subpopulations, isolation techniques, and diverse functions in cancer progression. *Frontiers in immunology*, *9*, 738.
- Wu, X., Hou, P., Qiu, Y., Wang, Q., & Lu, X. (2020). Large-scale analysis reveals the specific clinical and immune features of DGCR5 in glioma. *Onco. Targets. Ther.*, *13*, 7531–7543.
- Xu, W., Zhu, H., Gu, M., Luo, Q., Ding, J., Yao, Y., Chen, F., & Wang, Z. (2013). DHTKDI is essential for mitochondrial biogenesis and function maintenance. *Febs Letters*, *587*, 3587–3592.
- Yan, K., Wu, Q., Yan, D. H., Lee, C. H., Rahim, N., Tritschler, I., DeVecchio, J., Kalady, M. F., Hjelmeland, A. B., & Rich, J. N. (2014). Glioma cancer stem cells secrete Gremlin1 to promote their maintenance within the tumor hierarchy. *Genes & development*, *28*, 1085–1100.
- Yuana, Y., Sturk, A., & Nieuwland, R. (2013). Extracellular vesicles in physiological and pathological conditions. *Blood Reviews*, *27*, 31–39.
- Zaborowski, M. P., Balaj, L., Breakefield, X. O., & Lai, C. P. (2015). Extracellular vesicles: Composition, biological relevance, and methods of study. *Bioscience*, *65*, 783–797.
- Zhao, K., Cui, X., Wang, Q., Fang, C., Tan, Y., Wang, Y., Yi, K., Yang, C., You, H., Shang, R., Wang, J., & Kang, C. (2019). RUNX1 contributes to the mesenchymal subtype of glioblastoma in a TGFβ pathway-dependent manner. *Cell Death & Disease*, *10*, 877.
- Zhou, Y., Zhou, B., Pache, L., Chang, M., Khodabakhshi, A. H., Tanaseichuk, O., Benner, C., & Chanda, S. K. (2019). Metascape provides a biologist-oriented resource for the analysis of systems-level datasets. *Nature Communication*, *10*, 1523.
- Zhou, C., Jiang, X., Liang, A., Zhu, R., Yang, Y., Zhong, L., & Wan, D. (2020). COX10-AS1 facilitates cell proliferation and inhibits cell apoptosis in glioblastoma cells at post-transcription level. *Neurochemical Research*, *45*, 2196–2203.
- Zhou, K., Arslanturk, S., Craig, D. B., Heath, E., & Draghici, S. (2021). Discovery of primary prostate cancer biomarkers using cross cancer learning. *Science Reports*, *11*, 10433.
- Zohrabian, V. M., Forzani, B., Chau, Z., Murali, R., & Jhanwar-Uniyal, M. (2009). Rho/ROCK and MAPK signaling pathways are involved in glioblastoma cell migration and proliferation. *Anticancer Research*, *29*, 119–123.

## SUPPORTING INFORMATION

Additional supporting information can be found online in the Supporting Information section at the end of this article.

**How to cite this article:** Hsia, T., Yekula, A., Batool, S. M., Rosenfeld, Y. B., You, D. G., Weissleder, R., Lee, H., Carter, B. S., & Balaj, L. (2022). Glioblastoma-derived extracellular vesicle subpopulations following 5-aminolevulinic acid treatment bear diagnostic implications. *Journal of Extracellular Vesicles*, *11*, e12278. <https://doi.org/10.1002/jev2.12278>